ACADEMIA BIOLOGY

Research Article
Published: 2025-09-26
https://doi.org/10.20935/AcadBiol7907

Integrating classical and quantum mechanics in melatonin receptors for structure-guided drug design

Gabriela de Lima Menezes[1], Gabriel Vinícius Rolim da Silva[1], Katyanna Sales Bezerra[1,2], Marielena Vogel Saivish[3,4], Clara Sales Gurgel Ribeiro Dantas[5], Douglas Soares Galvão[2], John Fontenele Araújo[6], Jonas Ivan Nobre Oliveira[1], Roosevelt Alves da Silva[7], Umberto Laino Fulco[1,*]

Academic Editor: Andre J. van Wijnen

Abstract

Although melatonin receptor agonists are acknowledged for their therapeutic potential for managing sleep problems, the structural optimization of these compounds is made challenging by variations in crystallographic data. This study aims to improve the structure of the melatonin receptor type 1 and ramelteon (MT_1-RMT) complex and propose a new melatonin receptor agonist with an enhanced binding affinity. Molecular dynamics (MD) simulations have been used to improve the experimental MT_1-RMT complex, followed by quantum-mechanical (QM) calculations employing density functional theory (DFT) to assess ligand–receptor interactions. The MD simulations effectively optimized the MT_1-RMT complex, resulting in a conformation that was consistent with the experimental binding affinities. The QM calculations validated the improved binding affinity, and additional structural insights facilitated the rational design of a new agonist, N-[2-(5-methoxy-2-phenyl-1H-indol-3-yl)ethyl]propanamide (MPI), which exhibited better affinity for the MT_1 and melatonin receptor type 2 (MT_2) receptors. These findings suggest that MD-based refinement enhances the precision of protein–ligand complex models and that MPI is a suitable candidate for future pharmaceutical development. Subsequent research should examine the pharmacokinetic characteristics and in vivo effectiveness of MPI.

Keywords: *melatonin receptors, molecular dynamics, density functional theory, ab initio, drug design*

Citation: de Lima Menezes G, Rolim da Silva GV, Sales Bezerra K, Vogel Saivish M, Sales Gurgel Ribeiro Dantas C, Soares Galvão D, et al. Integrating classical and quantum mechanics in melatonin receptors for structure-guided drug design. *Academia Biology* 2025;3. https://doi.org/10.20935/AcadBiol7907

1. Introduction

Melatonin (MLT), chemically designated as N-acetyl-5-methoxytryptamine, is a neurohormone whose secretion is regulated by the presence or absence of light [1]. This control is initiated by a G protein-coupled receptor in the eye known as melanopsin, which responds to both natural and artificial light. It is located in the retinal ganglion cells (RGCs). In the presence of light, signals are transmitted to the suprachiasmatic nucleus (SCN), activating the RGCs and inhibiting melatonin production by the pineal gland. Conversely, when there is no light, the RGCs' signals to the SNC are suppressed, which causes melatonin to be produced and secreted [2, 3].

Melatonin receptors predominantly promote the action of melatonin in animal cells. They are classified into two subtypes: melatonin receptor type 1 (MT_1) and melatonin receptor type 2 (MT_2) G-protein-coupled receptors (GPCRs) [4, 5]. MT_1 and MT_2 are widely spread throughout the brain, cerebellum, ovary, testis, liver, kidney, cardiovascular system, skin, gallbladder, adipocytes, and colon [6–9]. They exhibit 55% sequence similarity and 70% when exclusively analyzing the transmembrane region. Furthermore, their main functions differ: MT_1 is in charge of the acute suppression of neuronal firing, while MT_2 is essential for effective phase-shifting [10].

Approximately 30–35% of adults experience insomnia, a sleep condition characterized by difficulties with beginning or maintaining sleep. This illness impacts individuals both physically and economically, as it is associated with reduced cognitive function and increased medical expenses on doctors and medications [11]. In addition to cognitive issues, insomnia has been identified as a factor that increases the risk of hypertension, type 2 diabetes mellitus, and mortality [12, 13]. Insomnia can be treated with both pharmacological and non-pharmacological methods. Non-pharmacological interventions include improvements to an individual's lifestyle and behavior, such as physical activity, proper sleep hygiene, sleep limitation, and relaxing strategies [14]. At the same time, pharmacological intervention includes sedative–hypnotics (such as Estalozam, Flurazepam, Zolpidem, Zaleplon,

[1]Department of Biophysics and Pharmacology, Federal University of Rio Grande do Norte, Natal, Brazil.
[2]Applied Physics Department, University of Campinas, Campinas, Brazil.
[3]Virology Research Laboratory, Department of Dermatological, Infectious and Parasitic Diseases, São José do Rio Preto School of Medicine, São José do Rio Preto, Brazil.
[4]Brazilian Center for Research in Energy and Materials, Campinas, Brazil.
[5]Department of Medicine, Potiguar University, Natal, Brazil.
[6]Department of Physiology and Behavior, Federal University of Rio Grande do Norte, Natal, Brazil.
[7]Special Unit of Exact Sciences, Federal University of Jataí, Jataí, Brazil.
*email: umbertofulco@gmail.com

and others), melatonin, and its analogs [15–17].

There is increasing interest in the therapeutic use of melatonin to treat insomnia, especially as a sleep inducer. However, several countries have not yet regulated the use of melatonin as a medicine, despite its widespread use as a food supplement. For example, exogenous melatonin is one of the most popular natural products taken by adults in the United States, and it is recommended by the American Academy of Sleep for the treatment of circadian rhythm sleep disorders [18]. However, the short half-life of melatonin ($t_{1/2}$ = 40 to 60 min) poses a challenge to its efficacy in treating important sleep disorders [19]. For this reason, strategies for enhancing its half-life time have been proposed over the years.

One approach involved creating a solution of slow-release melatonin, suggested to enhance sleep duration in individuals with sleep problems [20, 21]. Another possibility is the development of melatonin receptor analogs that simulate the effects of melatonin. Examples of analogs include ramelteon (RMT), agomelatine, tasimelteon, and 2-phenylmelatonin (2-PMT), among others [22, 23]. Melatonin receptor agonists are seen as safer alternatives, especially for people with comorbidities. Both strategies offer an enhanced molecular half-life, resulting in better efficacy.

An increase in the drug's half-life and efficacy is associated with various parameters, including the affinity energy between the target protein and the molecule [24, 25]. Regarding this, in silico studies aim to evaluate these interactions, which allow for an analysis at the atomic and electronic levels of the factors responsible for these interactions [26, 27]. This approach allows for the identification of critical interaction spots and the proposal of optimizations for drugs with established mechanisms, consequently saving time and resources.

A previous investigation using quantum techniques investigated the interaction of MT_1 and MT_2 receptors with the compounds melatonin (MLT), RMT, and 2-PMT [28]. This research successfully identified the main regions of the ligands that are critical for receptor affinity. Nonetheless, a limitation of the MT_1-RMT complex, which failed to align with the literature, restricted a more definitive investigation into drug optimization.

The use of molecular dynamics (MD) to refine the structures predicted by protein modeling software has long been established as one of the most successful approaches for this purpose [29]. In the past, the use of MD to refine low-resolution structures deposited into the Protein Data Bank (PDB) was frequently discussed. However, with advancements in crystallography techniques, the extensive validation required for structure submission, and the various homology modeling methods available, this option for refining experimentally resolved structures has received less attention in recent years [30, 31].

The goal of this study was to improve the crystallographic structure of MT_1 with RMT; investigate the new, improved complex in more detail; and, by combining new and old data, develop a new molecule that can interact with MT_1 and MT_2. Based on these observations, the primary hypothesis suggested that the crystallographic structure obtained in the experiment was not the conformation with the lowest energy or the highest affinity. To address this, MD simulations were performed using the same protocol previously applied to the melatonin receptor complexes with MLT [28], aiming to identify the conformation with the highest protein–ligand affinity. Quantum-mechanical (QM) calculations using density functional theory (DFT) were then conducted to confirm, through energy calculations, the affinity ranking of the ligands.

The results presented here suggest that MD successfully improved the conformation of the MT_1-RMT complex, producing data more consistent with the literature. The affinity ranking for the receptors was confirmed using QM, a more accurate method for protein–ligand energy calculations. Moreover, with this new and more accurate data, a novel molecule that exhibits a higher affinity energy than that of MLT, RMT, and 2-PMT was proposed.

2. Materials and methods

2.1. Refining the MT_1-RMT XFEL-derived protein–ligand complex conformation

2.1.1. Molecular dynamics simulation and QM/MM calculation

Molecular dynamics (MD) simulations of the complex obtained from the Protein Data Bank (PDB ID: 6ME2) were conducted to optimize the conformation of the RMT ligand within the MT_1 binding pocket since previous studies have shown results inconsistent with the literature [28]. Independent triplicate simulations were performed using GROMACS 2022 [32, 33]. Ligand parameters for the MD simulations were generated using the Bio2byte ACPYPE server [34], employing the Gasteiger charge method and General Amber Force Field 2 (GAFF2). The server provided all necessary topology and parameter files for the MD simulations in GROMACS. The Amberff99SB-ILDN force field was selected for the protein.

For each system, a cubic box with the TIP3P water model [35] was used, ensuring that each side of the box extended at least 12 Å from the solute atoms. Cl^- ions were added to neutralize the system. Before the production phase of the MD, a short 1 ns NPT equilibration without positional restraints on the protein was performed, followed by a 200 ns production run without conformational restraints on the protein. The MD simulations produced a total of 2000 conformations of the protein–ligand complex. The same protocol was applied in a previous study to the MLT-MT_1 complex [28]. Further details are provided in the Supplementary materials.

The gmx_MMPBSA program [36] was used to analyze the last 1000 conformations (corresponding to the final 100 ns) of the complexes from each MD simulation using QM/MM-GBSA (Quantum Mechanics/Molecular Mechanics—generalized Born surface area) binding free energy calculations. In the QM/MM-GBSA methodology, the binding free energy is computed using the following **Equation (1)**:

$$\Delta G_{bind} = \Delta E_{MM} + \Delta E_{SCF} + \Delta G_{solv} - T\Delta S \quad (1)$$

The MM term (ΔE_{MM}) encompasses the bonded energy components (ΔE_{bond}, ΔE_{angle}, and $\Delta E_{dihedral}$) and the nonbonded energy components (ΔE_{ele} and ΔE_{vdW}). The QM term (ΔE_{SCF}) includes the energy of atoms within the QM region, computed using semi-empirical QM Hamiltonians. The solvation energy term (ΔG_{solv}) is determined by the sum of the polar contribution to solvation free energy derived from the GB model (ΔG_{GB}) and the nonpolar

component obtained from a linear relationship with the solvent-accessible surface area (ΔG_{SA}).

For the QM/MM-GBSA calculations, the QM region was restricted to residues within 5 Å of the ligand, and the semi-empirical functional applied was PM6-DH+. Explicit solvent molecules and Cl- ions were excluded from the analysis, while an implicit solvent was used. Employing an implicit solvent model further decreases the computational cost by eliminating the noise introduced by explicit solvent molecules. Moreover, the removal of ions becomes necessary, as gmx_MMPBSA, which is based on AMBER's MMPBSA.py, utilizes implicit solvent models that are not parametrized to represent such atomic species [37] accurately. The lowest-energy complexes for each system were selected for QM calculations via DFT.

The MD trajectories were visualized using UCSF Chimera [38]. The root mean square deviation (RMSD) and fluctuation (RMSF) were calculated using the 'gmx' commands from the GROMACS package. These measures are crucial for evaluating the protein's overall stability (RMSD) along the trajectory and the average fluctuation per residue (RMSF). An unstable RMSD, characterized by fluctuating high and low values or values that escalate indefinitely over time, indicates that the protein destabilizes in solution. If the value remains constant throughout time, it indicates a highly stable protein. The mean value shown by the RMSF suggests areas of the protein exhibiting high flexibility when elevated and areas of poor flexibility when diminished. These two measures interrelate and validate one another. All plots were generated using the R language in RStudio 4.1.1 (http://www.rstudio.com/), and protein images were rendered using PyMol [39].

2.1.2. MFCC and quantum-mechanical calculations

For the QM calculations involving the RMT molecule, the lowest-binding-free-energy conformation of MT_1 from the QM/MM-GBSA analysis was selected. QM calculation is a precise methodology for studying ligand–protein interactions [40–45]. However, for large systems, the computational cost can be significantly high. To reduce these costs and make the calculations of the complexes feasible, the Molecular Fractionation with Conjugated Caps (MFCC) [46] scheme was applied. In summary, the MFCC scheme involves dividing the protein into individual amino acids by breaking the peptide bonds and calculating the interactions between each residue and the ligand separately. The sum of the individual amino acid energies provides an approximate binding energy for the entire complex. The MFCC approach employs 'caps' to complete the valence of the amino acids after breaking the peptide bonds at both the N-terminal and C-terminal ends. These caps consist of amino acid residues that precede and follow the main amino acid. Additionally, the caps help to reproduce the environment in which the amino acid resides better.

The following equation (**Equation (2)**) outlines the MFCC scheme for determining the interaction energy ($IE_{LIG/Ri}$) between the ligand (LIG) and the amino acid R^i, where i represents the *i-th* amino acid in the protein chain:

$$IE_{LIG/Ri} = E\left(LIG + C^{i-1}R^iC^{i+1}\right) - E\left(C^{i-1}R^iC^{i+1}\right) - E\left(LIG + C^{i-1}C^{i+1}\right) + E\left(C^{i-1}C^{i+1}\right) \quad (2)$$

The caps, denoted as C^{i-1} and C^{i+1}, refer to the adjacent residues that are covalently linked to the amine and carboxyl groups of R^i, respectively. The initial term ($E(LIG + C^{i-1}R^iC^{i+1})$) determines the interaction energy between the ligand LIG and the main residue (R^i) associated with the caps (C^{i-1} and C^{i+1}). MFCC aims to calculate the contributions of individual amino acids to the binding affinity. Consequently, the second and third terms are incorporated to separate the effect of the primary residue and remove the interaction energy between the binder and the caps. The second term ($E(C^{i-1}R^iC^{i+1})$) denotes the energy associated with the residue (R^i) linked to the caps (C^{i-1} and C^{i+1}), whereas the third term ($E(LIG + C^{i-1}C^{i+1})$) reflects the interaction energy between the LIG and the caps (C^{i-1} and C^{i+1}). The energies obtained from the second and third terms are subtracted from the first term to eliminate their impact on the energy interaction between LIG and R^i.

Due to the double subtraction of the caps' energies in the second and third terms, it is essential to reintegrate them into the fourth term ($E(C^{i-1}C^{i+1})$) to accurately reflect their influence on the energy interaction between LIG and R^i. This step precisely assesses the contribution of each individual amino acid to the overall binding affinity. Consequently, this approach makes it possible to calculate an approximate binding affinity for large systems, such as a protein–ligand complex.

After fragmenting the amino acids, the interaction energy between the receptor and the ligand was calculated using the Gaussian 16 package [47], which employs DFT formalism [48–50]. The simulations were performed using the generalized gradient approximation (GGA) with the B97D functional, which has proven to be an efficient and accurate QM method for large systems, especially when dispersion forces play a significant role [51]. To represent the Kohn–Sham orbitals for all electrons, a 6-311+G(d,p) triple-zeta valence basis set was applied, with an additional diffuse function (+) and polarization functions (d,p). The conductor-like polarizable continuum model (CPCM) was used to account for solvent effects in the QM calculations, with dielectric constants (ϵ) of 10 and 40. The constant of 40 is reported to resemble the crystalline environment [52, 53], while the constant of 10 was used here as a control, where a lower constant is expected to result in greater medium permissiveness and lower energy values. This ensures that the computations for both constants were accurately executed. Moreover, this QM methodology is identical to that employed for the XFEL structure, rendering the results substantially comparable.

2.2. The proposed new MT_1 and MT_2 agonists

2.2.1. MFCC and quantum-mechanical calculation

We determined the molecule's structure by analyzing the energy and interaction data for RMT^{MD} (which was obtained in this study) and 2-PMT, particularly the altered regions with respect to MLT. The primary alteration to 2-PMT was the incorporation of the phenyl ring, which constitutes the C ring (**Figure 1**). Based on Menezes et al. (2024) [28] study, this ring was determined to be significant in the interaction with Tyr281 (−3.05 kcal/mol). Due to this modification, the interaction between 2-PMT and MT_2 improved in comparison to that for MLT. The value changed from −2.84 kcal/mol to −4.12 kcal/mol for Val124 and from 0 to −4.07 kcal/mol for Tyr294, which was previously insignificant.

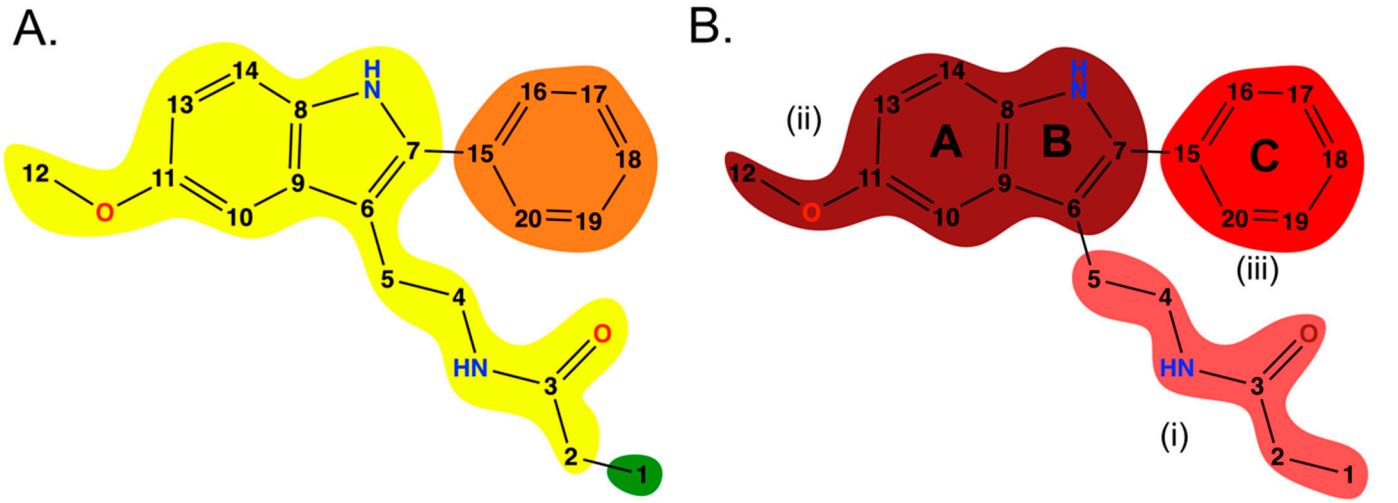

Figure 1 • A two-dimensional depiction of the MPI molecule. (**A**) The regions are designated by the following colors: yellow—MLT structure; green—RMT modification that significantly enhances affinity; and orange—2-PMT modification. (**B**) Segmentation of the molecule into three distinct sections (i, ii, and iii) in three different shades of orange–red to facilitate enhanced discussion and analysis of the results.

The incorporation of the -CH_3 group at position 1 of the MLT molecule in RMT significantly altered the affinity energy with the melatonin receptors. The primary interactions with the novel atom (C1) involved Leu254 (which decreased the energy from −1.98 kcal/mol in MLT to −3.63 kcal/mol in RMT^{MD}), Val111 (exhibiting an increase in affinity from −1.90 kcal/mol to −3.36 kcal/mol), and a more substantial contribution from the C1 atom, particularly in its interaction with Phe196 (which enhanced the affinity from −0.10 kcal/mol to −3.01 kcal/mol). Hence, the newly suggested molecule adhered to the foundational structure of MLT, incorporating the phenyl ring of 2-PMT at position 5 and a -CH_3 group at position 1, as illustrated in **Figure 1**. The chemical is designated as N-[2-(5-methoxy-2-phenyl-1H-indol-3-yl)ethyl]propanamide (hence referred to as MPI) and is indexed in PubChem under the identifier 10041816.

2.2.2. Molecular docking of MPI in MT_1 and MT_2

To assess the affinities of MT_1 and MT_2 with the MPI molecule, molecular docking, molecular dynamics, and QM/MM-GBSA calculations were used to identify the ideal complex structure and conformation. Consequently, we first retrieved the structures of the proteins. The MT_1 structure was obtained from the Protein Data Bank [54]. The crystal exhibiting the lowest resolution (6ME2 [55]) at 2.8 Å, indicating superior quality, was chosen for MPI docking. An identical method was followed for the MT_2 structure. The structure 6ME6 [56] was selected since it possesses the lowest resolution (2.8 Å) among the known MT_2 structures in the PDB.

The MT_1 and MT_2 proteins were cleaned, their chains were modified, and their energies were optimized on the Discovery Studios server before being converted into the PDBQT format as described. In this case, we removed artifacts from the crystallization process along with the associated RMT and 2-PMT ligands bound to MT_1 and MT_2, respectively. We additionally incorporated the absent side chains and hydrogen atoms. In accordance with the crystal extraction experiment, the PropKa 2.0 web server [57] was used to assess the protonation states of the MT_1 and MT_2 proteins at pHs of 7.0 and 7.4. After these modifications, AutoDock Tools was utilized for the conversion of larger molecules from PDB into PDBQT format [58].

The protonation of the molecule at pHs of 7.0 and 7.4, corresponding to the experimental pH of proteins, was confirmed using MarvinSketch code version 17.24 (Marvin Beans Suite—ChemAxon). The Meeko 0.6.1 tool [59] subsequently converted the molecule into PDBQT format.

The Uni-GBSA 0.1.6 tool, released in 2023 as a web server and open-source software, was utilized as a further phase following molecular docking [60]. Docking tools, such as AutoDock Vina, derive their scores (in kcal/mol) with limited accuracy by summing empirical energy terms, complicating the assessment of the binding affinity between two molecules. The Uni-GBSA program employs the MM/GB(PB)SA approach, which is more accurate, to calculate the binding free energy of the molecular docking outcomes.

2.2.3. Molecular dynamics simulation and binding energy calculations

To compare the results with the MLT, RMT, and 2-PMT molecules, the identical MD methodology utilized in the work by Menezes et al. (2024) [28] was applied here. For this purpose, the MT_1-MPI and MT_2-MPI complexes were chosen based on the Uni-GBSA methodology. The lower energy values of these complexes were chosen for MD simulations.

Following the same protocol, the final 100 ns of each MD trajectory underwent a QM/MM analysis, and the lowest-energy complexes for each system were chosen for QM computation employing the DFT method, as delineated in Section 2.1.2. The molecular structures obtained from MD and used for the DFT calculations and the input files for the MD and QM/MM calculations are available at Zenodo repository [61].

2.3. Quantum ligand properties

2.3.1. Geometric optimization

Initially, we obtained the chemical structures of MPI, RMT, 2-PMT, and MLT from the public databases ChemBL [62] and PubChem [63]. We utilized the BIOVIA Discovery Studio 2023 v.22 software on a dedicated server. We adjusted the ligands employing the "Clean Geometry" and "Minimize Ligands" tools. Furthermore, we conducted an extra geometric optimization employing the "Quick Minimization" and "Full Minimization" functions, applying the "Smart Minimizer" algorithm. Geometric optimization of each ligand was conducted using the "Calculate Energy (DFT)" tool, configured with Geometry Optimization parameters employing the PBE force field and water as the explicit solvent. The main goal of this step was to obtain ligands with the most effective geometry for the quantum analysis.

2.3.2. Molecular electrostatic potential

Molecular electrostatic potential (MEP) maps were constructed to assess the charge distribution of the studied compounds. MEP is characterized as the electrostatic potential of a molecule surrounding its surface, facilitating the identification of regions that have a distinct charge density. This tool allows for the visualization of the charge distribution and molecular features relevant to chemical reactivity, including the potential for specific interactions, such as electrostatic interactions. The electrostatic potential (V(r)) around a biomolecule is crucial for analyzing and predicting its reactivity [64, 65].

2.3.3. Quantum-chemical descriptors

Density functional theory (DFT) is a quantum technique frequently employed to enhance molecular efficacy in simulation analyses. It provides comprehensive information regarding the electronic behavior of molecules and their influence on parameters and descriptors in chemistry and quantum physics. The compounds analyzed—MLT, 2-PMT, RMT, and MPI—had their HOMO (Highest Occupied Molecular Orbital) and LUMO (Lowest Unoccupied Molecular Orbital) energies, HOMO-LUMO gap energy, ionization potential (I), electron affinity (A), chemical hardness (η), softness (S), chemical potential (μ), electronegativity (χ), and electrophilicity index (ω) computed [66, 67]. The mathematical equations for these parameters are delineated as [68]

- Ionization potential (I) is defined as $I = -E\_HOMO$;
- Electronic affinity (A): $A = -E\_LUMO$;
- Chemical hardness (η) is defined as $(I - A)/2$;
- Softness (S) is calculated as $S = 1/\eta$;
- Chemical potential (μ): $\mu = -(I + A)/2$;
- Electronegativity (χ): $\chi = (I + A)/2$;
- Electrophilicity index (ω): $\omega = \mu^2/(2\eta)$.

We computed these descriptors utilizing the B3LYP functional and the 6-31G(d,p) basis set. These descriptions provide valuable insights into the energy responses and reactive potential of each molecule inside chemical structures.

3. Results

3.1. Refined MT_1-RMT XFEL-derived protein–ligand complex conformation

The DFT calculations for the MT_1-RMT complex, as previously examined, do not align with the literature, which indicates that RMT has a higher affinity for the MT_1 receptor than MLT, and that RMT's affinity for MT_1 exceeds that for MT_2. The focus of the issue was primarily directed towards modifying this specific complex, as it is the only one among the six analyzed that does not correspond with the experimental results, utilizing MD simulations for this adjustment.

To differentiate the complexes with RMT, the experimentally obtained complex will be designated as MT_1-RMT^{XFEL}, while the complex derived from MD will be named MT_1-RMT^{MD}.

The RMSD result of the MT_1-RMT^{MD} complex is shown in **Figure 2**. Since interference from bacterial insertion regions had been previously observed to affect RMSD values, these regions were excluded from the current RMSD calculations. In **Figure 2A**, it is evident that the three replicates exhibited similar RMSD behavior, with values lower than those observed when the insertion regions were included. However, during the initial phase of the simulations (up to approximately 64 ns), larger fluctuations (ranging from 0.27 nm to 0.55 nm) were observed, suggesting initial conformational adjustments during the MD.

Between 65 ns and 160 ns, moderate fluctuations in the RMSD (0.37 nm to 0.53 nm) were noted, particularly in replicates 1 and 2, indicating that replicate 3 displayed greater stability compared to the others. By the end of the simulation, all three replicates had reached stability. Replicate 1 had RMSD values around 0.42–0.45 nm, replicate 2 values around 0.44 nm, and replicate 3 values around 0.37 nm. However, it is notable that replicate 3, after a period of stability (until 184 ns), saw a reduction in the RMSD from 0.5 nm to around 0.37 nm by the end of the MD.

The average RMSD value of the three replicates is shown in **Figure 2A** (black line). It is evident that on average, the replicates were quite stable throughout the 200 ns trajectory. These results suggest that the MD was suitable for the objective of obtaining stable structures of the MT_1-RMT complex in an aqueous environment. The RMSF analysis, also excluding the bacterial region, shows quite similar values among the replicates, as illustrated in **Figure 2B**.

The QM/MM-GBSA analysis of the last 100 ns (1000 conformations) from the three replicates reveals that the conformations in all three simulations had affinities lower than 0 kcal/mol, with the majority below −5 kcal/mol, indicating that all conformations in the latter half of the MD exhibited favorable interaction energies (**Figure 2**). It is important to note that there was a significant drop in the affinity energies in the complexes of replicate 3, particularly after 140 ns (conformation 1400). This observation is likely due to conformational adjustments between the protein and ligand that occurred during the MD simulation, resulting in the lowest-energy complex (−29.25 kcal/mol) among the 3000 analyzed conformations.

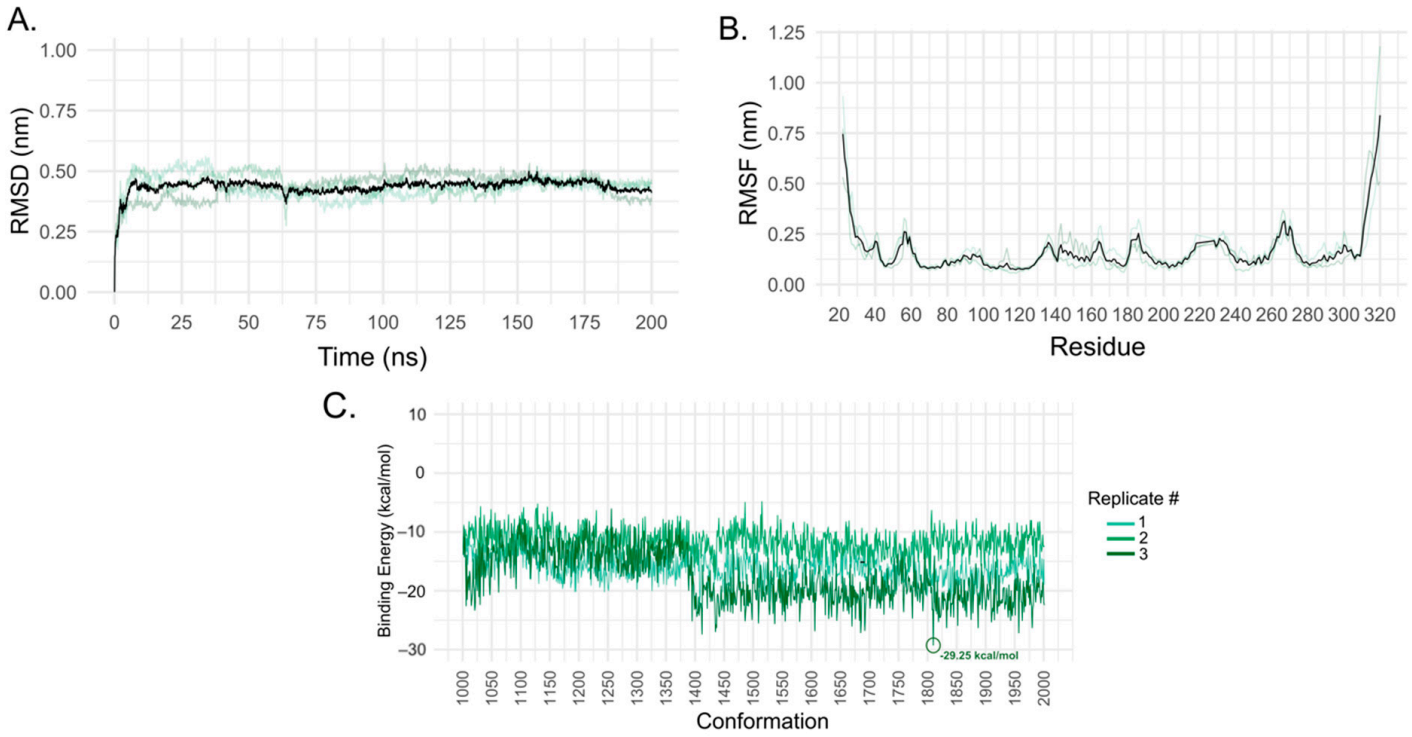

Figure 2 • RMSD and RMSF analysis of the MT_1-RMT^{MD} complex during 200 ns of MD simulation. (**A**) The RMSD of the three replicates displayed transparently, with the mean highlighted as a solid black line. (**B**) The RMSF of the three replicates displayed transparently, with the mean highlighted as a solid black line. In both analyses, the protein backbone was considered for the calculations. Individual RMSD and RMSF plots can be seen in Figures S1 and S2, respectively. (**C**) QM/MM-GBSA analysis of the last 1000 conformations (100 ns) from each replicate obtained through MD simulation.

The complex with the lowest binding free energy obtained through QM/MM-GBSA calculations was subjected to fragmentation following the MFCC methodology for DFT calculations, as previously applied to the other complexes [28]. The convergence graph, comparing MT_1-RMT^{MD} with melatonin (MT_1-MLT), ramelteon (MT_1-RMT^{XFEL}), 2-phenylmelatonin (MT_1-2-PMT), and MT_2-RMT from a previous study, is shown in **Figure 3**. In **Figure 3A**, the total energy of the complexes with the three ligands bound to MT_1 was evaluated. In this case, it is observed that the MT_1-RMT^{MD} complex has an intermediate energy value (−57.84 kcal/mol) between those of the MLT and 2-PMT complexes. Also, the MT_1-RMT^{MD} complex obtained here, with an energy of −57.84 kcal/mol, showed greater affinity than that of the experimental RMT complex with MT_2, which had an energy of −48.75 kcal/mol (**Figure 3B**).

In **Figure 3C**, it is evident that specific changes in interactions were crucial in reducing the binding energy of RMT, thereby increasing its affinity for the receptor. Notably, for Asn255, despite interacting with the same atom of the ligand, its interaction energy was reduced from −1.27 kcal/mol to −6.33 kcal/mol. Another significant interaction was with Thr178, which lowered the energy from −1.07 kcal/mol to −3.24 kcal/mol. In the MT_1-RMT^{MD} complex, Phe179 shifted to associate with a new region, interacting with ring [B] instead of atom i(C1). However, this alteration did not result in a significant change in binding energy compared to that for the MT_1-RMT^{XFEL} complex. Leu254, which had previously shown a repulsive interaction, now showed a negative interaction energy (−3.63 kcal/mol) with the i(C1) atom of RMT.

When comparing the key amino acids in the MT_1-RMT^{XFEL} complex with those in MT_1-RMT^{MD} (**Figure 3D**), an increase in the affinity of residues previously identified as crucial, such as Phe179, Val191, Gly108, Val111, and Ile112, was observed. Conversely, some amino acids exhibited an increase in binding energy (reduced affinity), including Gln181, Tyr281, and Val159, suggesting that these residues are not as essential as those previously mentioned. Asn162, however, maintained its energetic contribution unchanged between the two complexes.

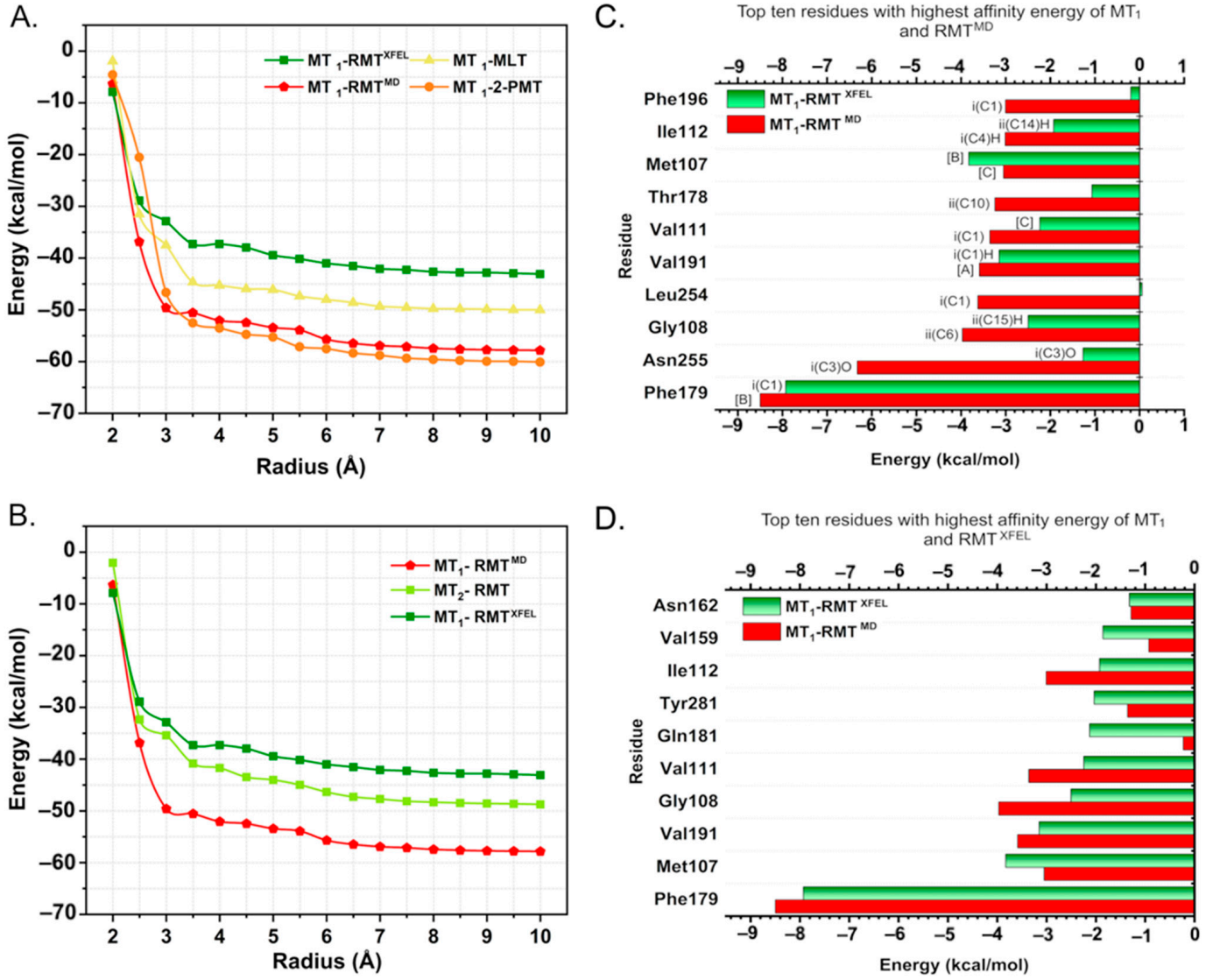

Figure 3 • (**A**,**B**) A convergence graph comparing the MT_1-RMT^{MD} complex with previously described complexes [28] formed by RMT, MLT, and 2-PMT. (**A**) Total energy as a function of the radius for the MT_1-RMT^{MD}, MT_1-RMT^{XFEL}, MT_1-MLT, and MT_1-2-PMT complexes. (**B**) Total energy as a function of the radius for the MT_1-RMT^{MD}, MT_1-RMT^{XFEL}, and MT_2-RMT complexes. (**C**,**D**) Graphical panels highlighting the key residues involved in the interaction between the MT_1 protein and the ligands RMT^{MD} (red bar) and RMT^{XFEL} (green bar). (**C**) A comparative graph of the 10 amino acids that contributed the most to the interaction in the MT_1-RMT^{MD} complex, showing the respective binding energies and the regions of the ligand involved. The graph also displays these same energies for the MT_1-RMT^{XFEL} complex. The absence of certain ligand regions in the MT_1-RMT^{XFEL} complex is due to the lack of significant contributions from nearby atoms to the overall binding affinity. (**D**) A comparative graph of the 10 amino acids that contributed the most to the interaction in the MT_1-RMT^{XFEL} complex. The structure of RMT with the atom designations and regions can be seen in Figure S3. All data are presented using a dielectric constant of $\epsilon = 40$.

Figure 4 highlights the key interactions between amino acids that contributed most to the binding affinity, shedding light on the critical protein–ligand interactions responsible for lowering the energy of the complex. In **Figure 4A**, Phe179 establishes two interactions with the [B] ring of the RMT molecule: a pi–sigma interaction (2.44 Å) and a pi–pi interaction (4.97 Å). Notably, in the MT_1-RMT^{XFEL} complex, only one interaction with the i(C1) atom was identified. This change resulted in a slight decrease in the interaction energy between this amino acid and the ligand in the MT_1-RMT^{MD} complex. The amino acid Thr178 increased its affinity for the complex by forming a dipole–dipole interaction with the ii(C10) atom of RMT (**Figure 3C** and **Figure 4A**).

Leu254, which exhibited repulsive energy in the experimental complex, now displays attractive energy through the formation of an alkyl–alkyl interaction with the i(C1) atom of the RMT molecule at a distance of 4 Å (**Figure 4B**). Another amino acid interacting with this same atom, contributing to a significant reduction in the interaction energy, is Phe196, which forms a pi–alkyl interaction at a distance of 4.35 Å (**Figure 4B**). Met107 was one of the few amino acids whose interaction energy increased, reducing its affinity for RMT by forming a pi–alkyl interaction with the [C] ring at a distance of 5.4 Å (**Figure 4B**), instead of the previous pi–sulfur interaction with the [B] ring seen previously. Nevertheless, Met107 remains one of the most relevant residues to affinity with RMT.

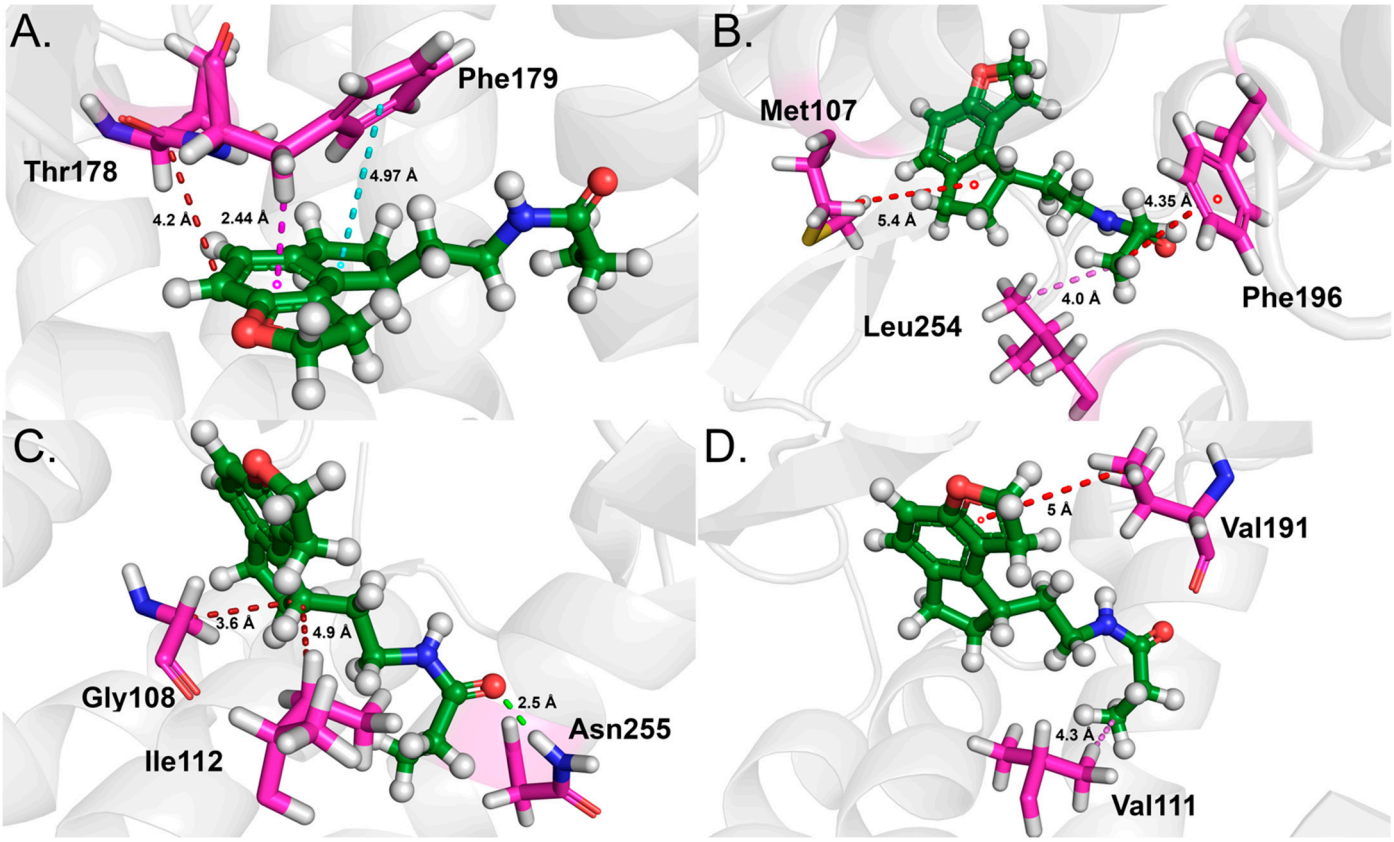

Figure 4 • Three-dimensional binding mode of RMT in the MT_1 structure of the MT_1-RMT^{MD} complex. (**A**) An interaction analysis between RMT and the amino acid residues: Phe179 and Thr178. (**B**) An interaction analysis between RMT and amino acid residues: Met107, Phe196, and Leu254. (**C**) A representation of the interaction analysis between RMT and the Gly108, Ile112, and Asn255 amino acids. (**D**) An interaction analysis between the RMT ligand and the Val191 and Val111 amino acids. In all panels, the ligand is represented by a dark green ball-and-stick, and the main MT_1 amino acids are shown as pink sticks. The types of interactions are color-coded: cyan for pi–pi, brown for dipole–dipole, red for pi–alkyl, purple for pi–sigma, and pink for alkyl–alkyl interactions.

Another amino acid that stands out significantly in the MT_1-RMT^{MD} complex, showing a much higher affinity compared to that for the MT_1-RMT^{XFEL} complex, is Asn255. In this complex, a 2 Å hydrogen bond forms with the i(C3)O atom of RMT (**Figure 3C** and **Figure 4C**). Since hydrogen bonds are strong interactions, this intermolecular bond significantly reduced the energy calculated for the complex. The conformational adjustment promoted by the MD simulation brought the amino acid closer to the ligand, allowing a hydrogen bond to form, whereas previously, the distance between them was 3.5 Å. Moreover, Ile112 forms a dipole–dipole interaction with the i(C4) atom at a distance of 4.9 Å (**Figure 4C**), also contributing to an increase in the complex's affinity.

Gly108 exhibits a dipole–dipole interaction with the ii(C6) atom at a distance of 3.6 Å (**Figure 4C**). Val111 shifted from interacting with the [C] ring to interacting with the i(C1) atom through an alkyl–alkyl interaction at 4.3 Å (**Figure 4D**), reducing the interaction energy and increasing the affinity. Val191, which previously engaged with the hydrogen associated with the i(C1) atom, now interacts with the [A] ring; nonetheless, this did not lead to a substantial alteration in affinity, which did see a slight enhancement (**Figure 4D**).

3.2. The proposed new melatonin receptor agonist

3.2.1. Molecular docking and molecular dynamics simulation of MT_1-MPI and MT_2-MPI complexes

MPI was synthesized and tested in 1995 in chicken brain cells and melanophore cells of *Xenopus laevis*, a species of anuran amphibian [69], along with other melatonin agonists. This study concluded that MPI has a high affinity for the receptors in chicken brains, greater than that of MLT itself. However, this study did not distinguish between the types of receptors. Moreover, there are no further reports in the literature exploring the efficacy of this molecule in human melatonin receptors. Therefore, based on the results described previously in this work, the affinity of MPI, as a potentially promising molecule for the treatment of insomnia, for the MT_1 and MT_2 receptors was evaluated.

Figure 5A illustrates the score distribution for the 1000 complexes generated using AutoDock Vina. Unlike the other molecules, particularly MLT, for which an identical methodology was adhered to, MPI exhibits a higher affinity for MT_2 than that for MT_1. Upon comparison of the results for MLT and MPI, it is evident that MPI has a higher affinity for both receptors, with values of −9.70 kcal/mol and −9.80 kcal/mol for MT_1 and MT_2, respectively (**Table 1**).

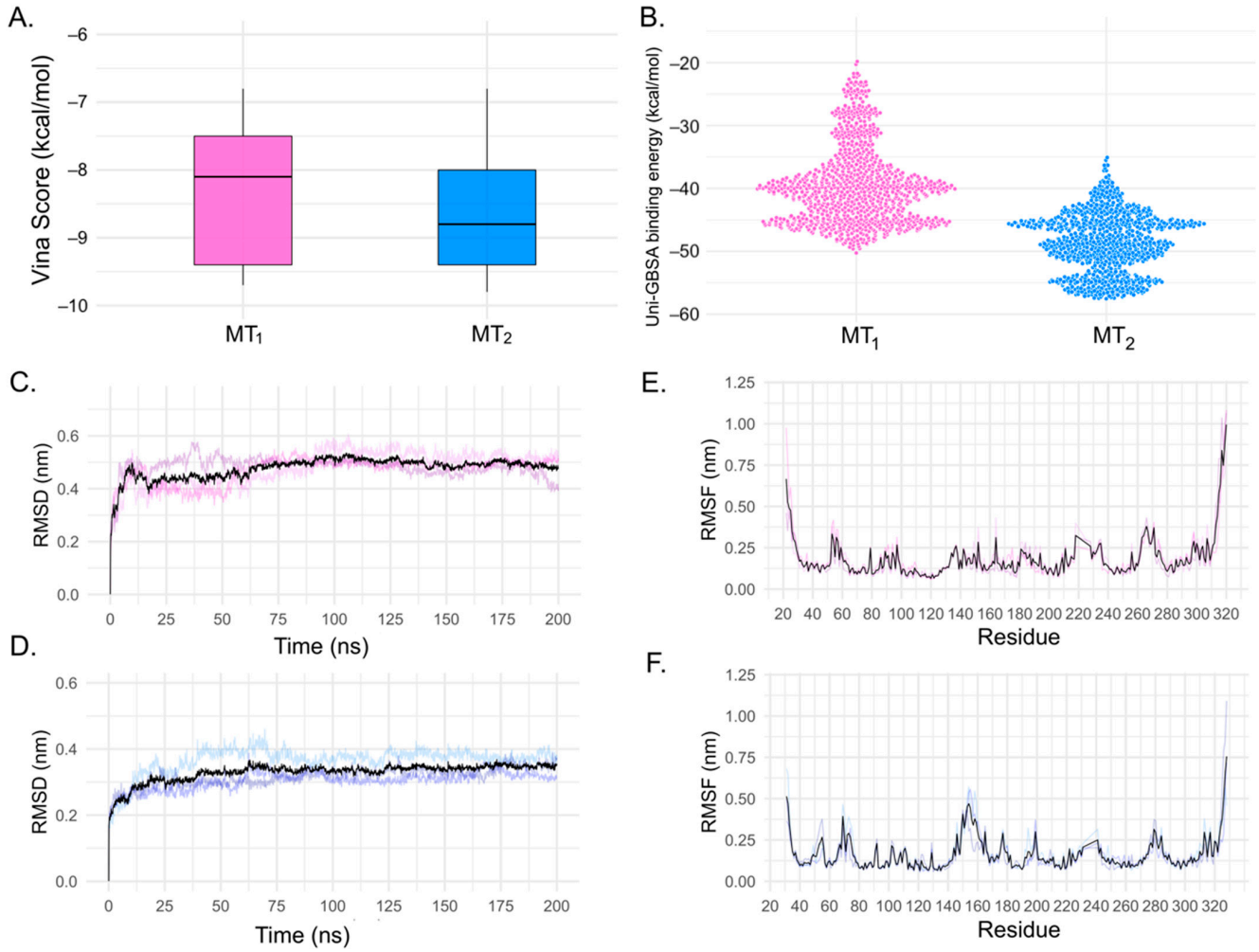

Figure 5 • MPI docking at MT_1 and MT_2 receptors and MD simulations. (**A**) A box plot of the distribution of the Vina scores in kcal/mol. The pink box is related to the MT_1–MPI complex, and the blue one pertains to the MT_2–MPI coupling. (**B**) The distribution of energies calculated by the Uni-GBSA program in kcal/mol. The pink dots are related to the MT_1–MPI complex, and the blue ones pertain to the MT_2–MPI complex. (**C**–**F**) RMSD and RMSF plots for 200 ns of the three replicates obtained in the MD simulations of the MT_1–MPI (pink lines) and MT_2–MPI (blue lines) complexes. In each plot, black lines represent the average values of three replicates. (**C**,**E**) RMSD and RMSF plots of the MPI complex with MT1. Individual RMSD and RMSF plots can be seen in Figures S4 and S5, respectively. (**D**,**F**) RMSD and RMSF plots of the MLT complex with MT_2. Individual RMSD and RMSF plots can be seen in Figures S6 and S7, respectively. In the RMSD and RMSF analyses, the protein backbone was considered for the calculations.

Table 1 • A summary of the results of the MPI anchoring performed using the Vina and Uni-GBSA programs.

Program	Receptor	Min.	Q1 [&]	Median	Average	Q3 [#]	Max.	SD. [†]
Vina	MT_1	−9.70	−9.40	−8.10	−8.39	−7.50	−6.80	0.9686
	MT_2	−9.80	−9.40	−8.80	−8.75	−8.00	−6.80	0.7713
Uni-GBSA	MT_1	−50.26	−44.71	−40.20	39.40	−36.61	−19.82	6.2560
	MT_2	−57.54	−51.76	−48.39	−48.57	−45.30	−35.08	4.6733

[&] Q1: first quartile; [#] Q3: third quartile; [†] SD: standard deviation.

The RMSD and RMSF studies omitted the bacterial insertion sites from the computation of these metrics, similar to the approach taken for the MT_1–RMT^{MD} complex. The MT_1–MPI (**Figure 5C,E**) and MT_2–MPI (**Figure 5D,F**) complexes are shown in **Figure 5**. **Figure 5C** illustrates the RMSD for each replication alongside the average derived from the three independent simulations. Stability for the three replicates was obtained at different intervals: replicate 3 exhibited stability from the onset of the simulation (~50 ns), while replicate 2 stabilized at around 75 ns—with both exhibiting values near 0.5 nm—and replicate 1 achieved stability near 90 ns (~0.55 nm). All replicates had results that closely aligned with the average following the 100 ns interval. The RMSF exhibits (**Figure 5E**) the most significant changes in the N- and C-terminal regions, with minor peaks identified between amino acids 50 and 60, 220 and 240, and 260 and 270 across the three replicates, reflecting the behavior noted in the MT_1–RMT^{MD} complex.

Figure 5D illustrates the RMSD of the three replicates alongside the average of the MT_2–MPI complex. The replicates had analogous behavior, all maintaining stability for around 75 ns of the simulation, with values ranging from 0.3 nm to 0.4 nm. The average reveals the significant stability achieved in the three runs. The RMSF results (**Figure 5F**) exhibited significant similarity across repetitions. Note the anticipated significant variations in the N- and C-terminal areas, along with a peak occurring between amino acids 145 and 165, which constitutes a loop region linking the TM3 and TM4 domains. In comparison to the MT_2–MLT complex, this RMSF result indicated a complex exhibiting fewer variations across all replicates. In conclusion, the replicas for MT_1–MPI and MT_2–MPI are truly positive, suggesting that what is expected to occur is most likely to occur in the actual system.

Figure 6 illustrates the energy analysis conducted via QM/MM on the final 500 conformations of the MD. These pertain to the final 50 nanoseconds, during which the clones exhibited greater stability. It is noteworthy that for both complexes (MT_1–MPI and MT_2–MPI), all energies are negative, indicating that all conformations are beneficial in energy terms and occur spontaneously. In the MT_1–MPI complex (**Figure 6A**), the distinction between the replicas in relation to their energy is clear. Replica 2 presented the highest average energy among the replicas, followed by that of replica 3 and replica 1. The MD of replica 1 precisely obtained the conformation with the lowest energy, which corresponded to conformation 1572 and had a value of −31.8 kcal/mol. Among the replicas of the MT_2–MPI complex (**Figure 6B**), this difference between the replicas is also noted, with replica 1 having the highest energy, replica 2 having intermediate energy values, and replica 3 having the lowest values. The conformation with the lowest energy was found for replica 3 of MT_2–MPI, with a value of −25.92 kcal/mol, which is the same as that for structure 1638 for MT_1–MPI. These data suggest a greater affinity of MPI for MT_1 than MT_2. Consequently, we selected these two complexes for the DFT analysis using MFCC, following the previous description of the other complexes.

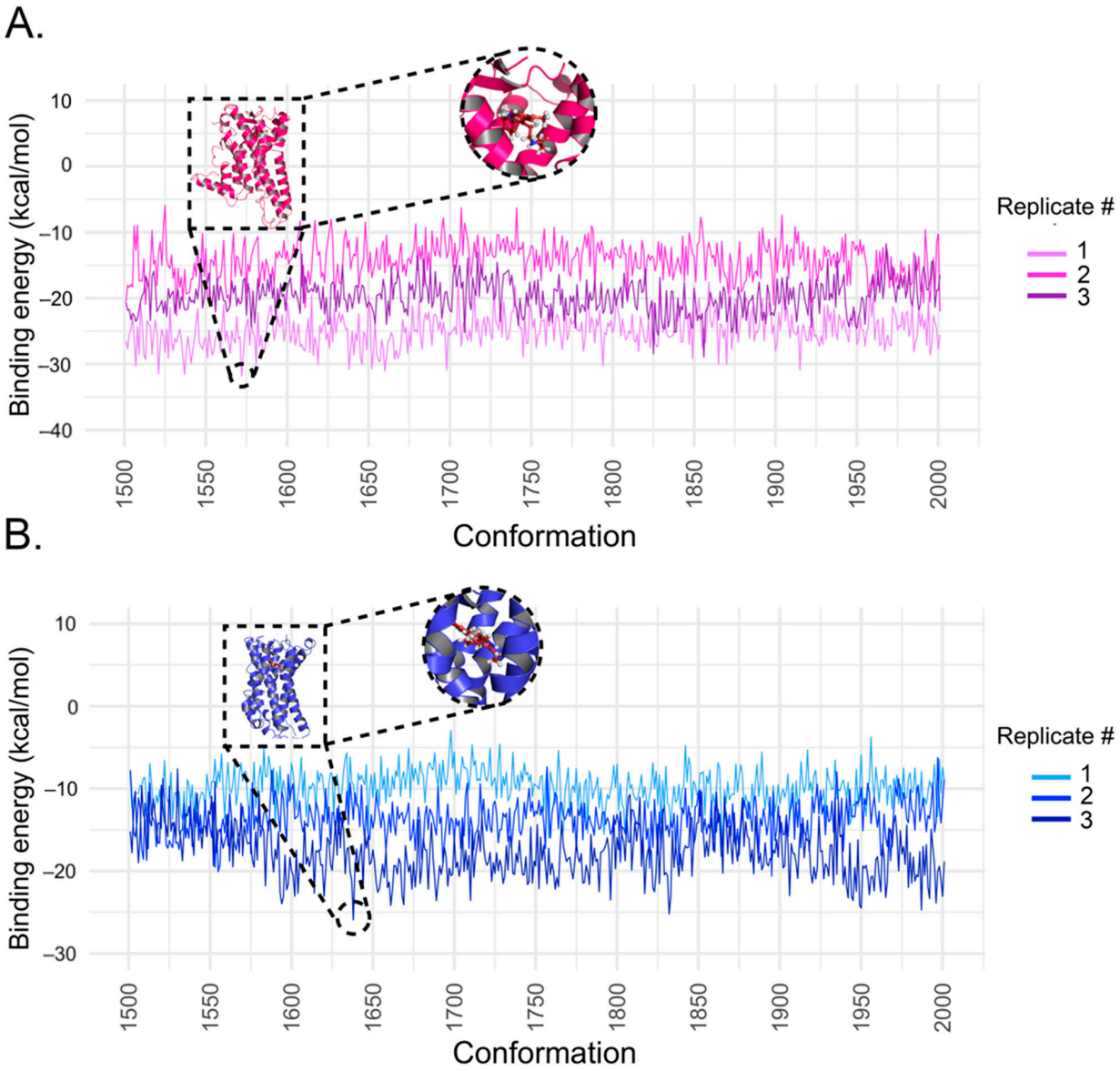

Figure 6 • QM/MM values along the MD trajectory of the last 50 ns. (**A**) Three replicas of MT_1–MPI, with the pink cartoon highlighting the lowest-energy complex corresponding to conformation 1572. (**B**) Replicas of MT_2–MPI, with the blue cartoon highlighting conformation 1638. In both highlights, the MPI ligand is represented in dark red as sticks and balls.

3.2.2. Quantum-molecular calculations of binding energy of MT_1-MPI and MT_2-MPI complexes

The interactions of the MT_1-MPI and MT_2-MPI complexes were studied by first looking at the energy as a function of the radius, following the same steps that were used for the other complexes. This can be seen in **Figure 7A**. In it, it is possible to observe the values for the two dielectric constants (ϵ = 10 and ϵ = 40). Looking at these data, the constant ϵ = 10 is confirmed to have a lower energy value than the constant ϵ = 40, indicating that the calculations were performed properly. Also, all dielectric constants and complexes show convergence between radii of 8 Å and 9 Å. This means that the amino acids with the highest interaction energy are in the range of up to 10 Å (**Figure 7A**).

For the MT_1-MPI complex, the energies found for ϵ = 10 and ϵ = 40 in a circle with a radius = 10 Å were −63.75 kcal/mol and −62.51 kcal/mol, respectively (**Figure 7A**). These energies covered 99 amino acids. We found that this value had the lowest energy when interacting with MT_1 among the four molecules in this study (MLT, RMT, 2-PMT, and MPI) (**Table 2**). This means that this molecule is the best one for binding to the MT_1 receptor.

The energies of the MT_2-MPI complex were found to be −67.84 kcal/mol (−66.75 kcal/mol) for dielectric constants of ϵ = 10 (ϵ = 40), which covers 98 amino acids up to 10 Å in diameter (**Figure 7A**). Again, this was the lowest energy value in the interaction with the MT_2 receptor among the molecules analyzed in this study (**Table 2**).

The main amino acids involved in the interaction with the MPI molecule can be observed in **Figure 7B**. For the MT_1-MPI complex, the order of the decreasing affinity and calculated energy (in kcal/mol, ϵ = 40) was Met107 (−5.64) > Phe179 (−5.10) > His195 (−4.57) > Gly108 (−4.23) > Phe251 (−3.44) > Ala104 (−3.43) > Leu254 (−3.07) > Asn162 (−3.07) > Val191 (−2.54) > Phe196 (−2.27) > Phe105 (−2.10) > Tyr285 (−2.06) > Val111 (−2.06) > Val159 (−1.98) > Tyr281 (−1.96). The MT_2 amino acids interacting with the MPI molecule (**Figure 7C**) in decreasing order of affinity and interaction energy (in kcal/mol, ϵ = 40) were Phe192 (−9.47) > Gly121 (−4.98) > Asn175 (−4.67) > Asn268 (−3.57) > Phe264 (−3.41) > Val124 (−3.38) > Tyr294 (−3.29) > Leu172 (−3.02) > Ile125 (−2.91) > Met120 (−2.81) > Leu181 (−2.10) > Val205 (−1.96). The main interactions performed by the most relevant amino acids to the affinity energy in these two complexes will be described below.

In **Figure 8**, we can see the interactions with the ten amino acids of the MT_1 protein with the highest affinity for the MPI molecule. In **Figure 8A**, Asn162 (−3.07 kcal/mol) is observed to form a 2 Å hydrogen bond with the oxygen in region ii. This same interaction is observed for MLT, which has this region in common with MPI. Once more, Phe179 (−5.10 kcal/mol) stands out in this complex. It has a pi–pi interaction with the aromatic ring [A] (**Figure 8A**) at a distance of 5.4 Å, which is also in the same area as MLT and 2-PMT. However, these molecules exhibit two pi–pi interactions, each with a lower affinity energy. The amino acid Leu254 (−3.07 kcal/mol) has a pi–alkyl interaction with the MPI molecule on the [C] ring, which is part of 2-PMT (**Figure 8A**). The other type is an alkyl–alkyl interaction on carbon i (C1), which is part of RMT. Only RMT exhibits this interaction.

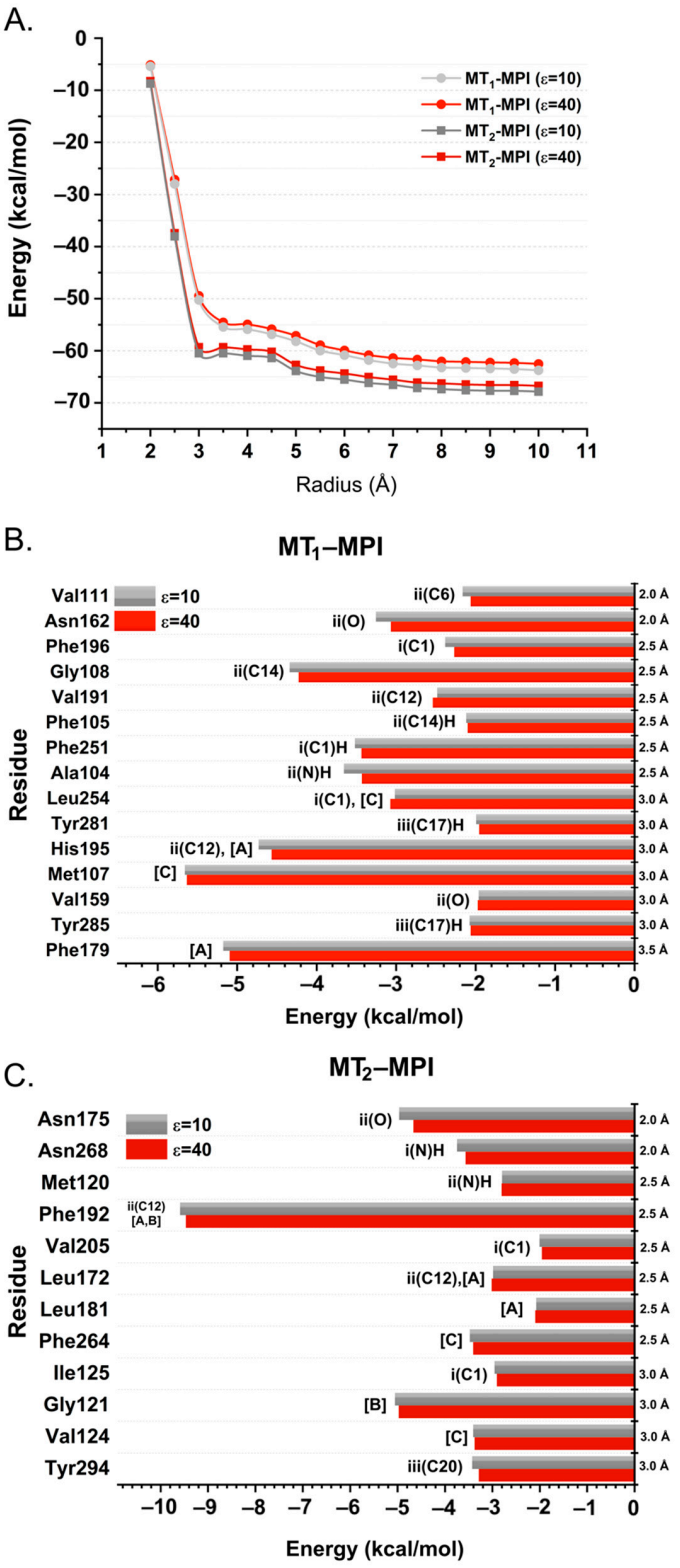

Figure 7 • The quantum-calculation results for MT_1-MPI and MT_2-MPI complexes. (**A**) A graphical representation of the total interaction energy of the MT_1 and MT_2 complexes with MPI for both dielectric constants (ϵ = 10 and ϵ = 40) as a function of the binding pocket radius calculated using the DFT/MFCC approach. (**B**,**C**) Graphical panels showing the most important residues for the interaction of MT_1 with MPI (light red and light gray bars for dielectric constants ϵ = 40 and ϵ = 10, respectively) and MT_2 with MPI (dark red and dark gray bars for dielectric constants ϵ = 40 and ϵ = 10, respectively). In addition, the region (i, ii, or iii), atom, and ring (based on the schematic representation in **Figure 1B**) that interact with each residue in the binding site can be seen on the left side of the bars. On the right side, the radius (in Å) at which that amino acid is relative to the ligand is shown.

Table 2 • Quantum-chemical results on binding energy between MT_1 and MT_2 and respective compounds (MLT, RMT, 2-PMT, and MPI).

Compound	MT_1	MT_2
MLT	−50.01 kcal/mol [&]	−44.26 kcal/mol [&]
RMT	−57.84 kcal/mol	−48.65 kcal/mol [&]
2-PMT	−60.09 kcal/mol [&]	−54.71 kcal/mol [&]
MPI	−62.51 kcal/mol	−66.75 kcal/mol

[&] Calculations performed by Menezes et al. (2024) [28].

Val191 (−2.54 kcal/mol) performs an alkyl–alkyl interaction with the ii (C12) atom at a distance of 3.6 Å (**Figure 8B**). Val191 also interacts with MLT and 2-PMT in this region but by performing a dipole–dipole interaction with the hydrogen bonded to ii (C12). Met107, which already stood out in the previous complexes, was the amino acid that presented the greatest affinity for MPI (−5.64 kcal/mol), performing a pi–alkyl interaction with the [C] ring at a distance of 3.6 Å (**Figure 8B**).

Gly108 (−4.23 kcal/mol) also stood out in this complex, with two pi–hydrogen interactions (one in each ring [A] and [B]) (**Figure 8C**), a weak type of non-conventional hydrogen bond that occurs X-H···π, where X = C, N, O. This type of interaction has been described as of great importance to biological systems [70, 71]. His195 (−4.57 kcal/mol) performs two interactions with MPI, one pi–pi interaction (5.5 Å) with ring [A] and another pi–alkyl interaction (4.7 Å) with the ii atom (C12) (**Figure 8C**). Although this is a common region of MLT, this is the first time that His195 has appeared as one of the main amino acids in the interaction with MT_1.

Ala104 (−3.43 kcal/mol) establishes a hydrogen bond with the ii(N)H atom at a distance of 2.5 Å (**Figure 8D**). Like His195, this amino acid was similarly notable in this combination for having a higher affinity for the ligand. Phe196 (−2.27 kcal/mol), noteworthy for its interaction with RMT^{MD} at the i(C1) atom, also exhibited a significant interaction in the MT_1-MPI complex at the same atom. **Figure 8D** illustrates the pi–alkyl interaction between Phe196 and MPI, measured at a distance of 5.2 Å. Phe251 (−3.44 kcal/mol), the amino acid exhibiting the fifth best interaction energy and not previously configured among the main amino acids, also demonstrated a non-conventional hydrogen bond interaction with the i(C1) atom (**Figure 8D**).

The main interactions with MT_2 can be observed in **Figure 9**. **Figure 9A** illustrates that Phe192 exhibits the highest affinity for MT_2 at −9.47 kcal/mol, a value supported by three interactions: two pi–pi interactions with rings [A] (5.2 Å) and [B] (5.5 Å), similar to the interactions of Phe192 with 2-PMT [28], and one pi–alkyl interaction with the ii (C12) atom at 4.9 Å. Asn175 (−4.67 kcal/mol) exhibited the third highest affinity for MT_2, establishing a hydrogen bond with the ii (C12) atom at 2.0 Å (**Figure 9A**), comparable to the interaction by Asn268 (−3.57 kcal/mol)—the amino acid with the fourth highest affinity—with the i(N)H atom at the same distance (**Figure 9B**).

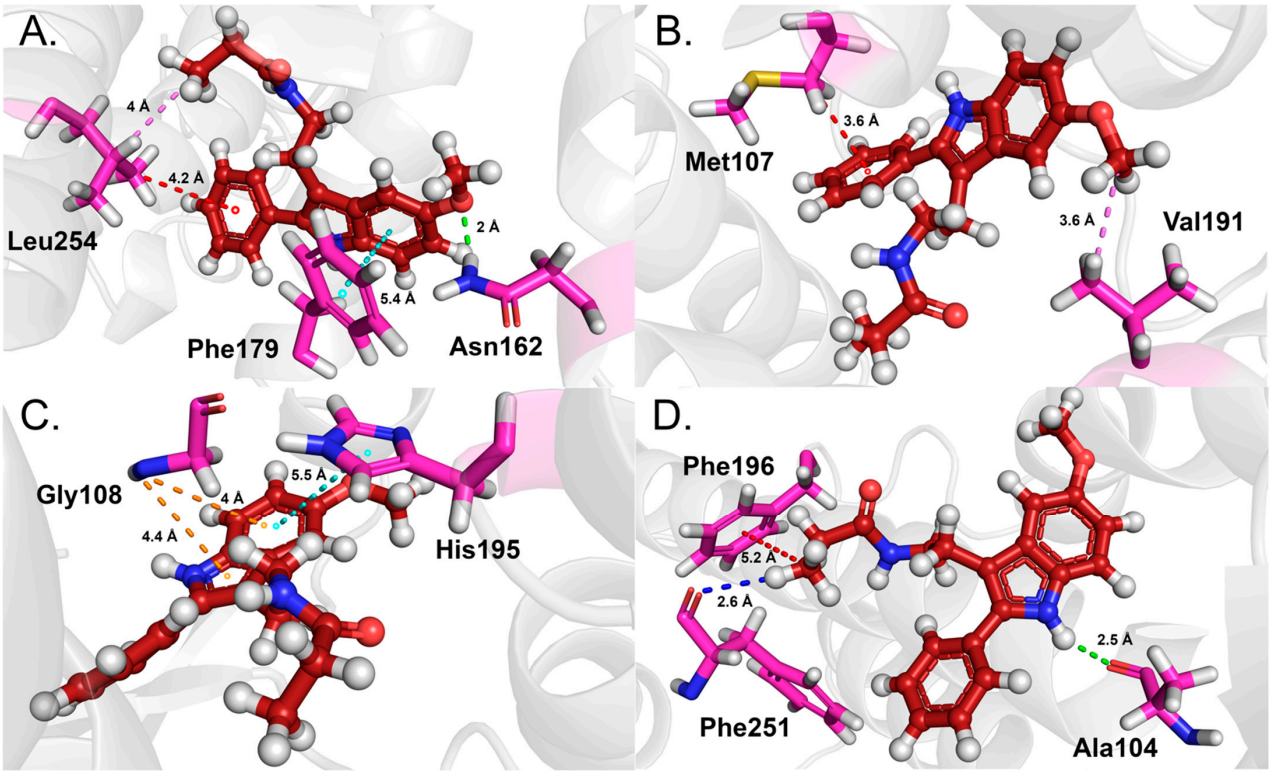

Figure 8 • An interaction analysis of the main amino acids in the MT_1-MPI complex. (**A**) An interaction analysis between MPI and the amino acid residues Asn 162, Phe179, and Leu254. (**B**) An interaction analysis between MPI and amino acid residues Met107 and Val191. (**C**) A representation of the interaction analysis between MPI and the Gly108 and His195 amino acids. (**D**) An interaction analysis between the MPI ligand and the Ala104, Phe196, and Phe251 amino acids. In all panels, the ligand is represented by a dark red ball-and-stick, and the main MT_1 amino acids are shown as pink sticks. The interaction type is colored as follows: pi–pi interaction (cyan); hydrogen bond (green); non-conventional hydrogen bond (dark blue); pi–alkyl interaction (red); alkyl–alkyl interaction (pink); and pi–hydrogen interaction (orange).

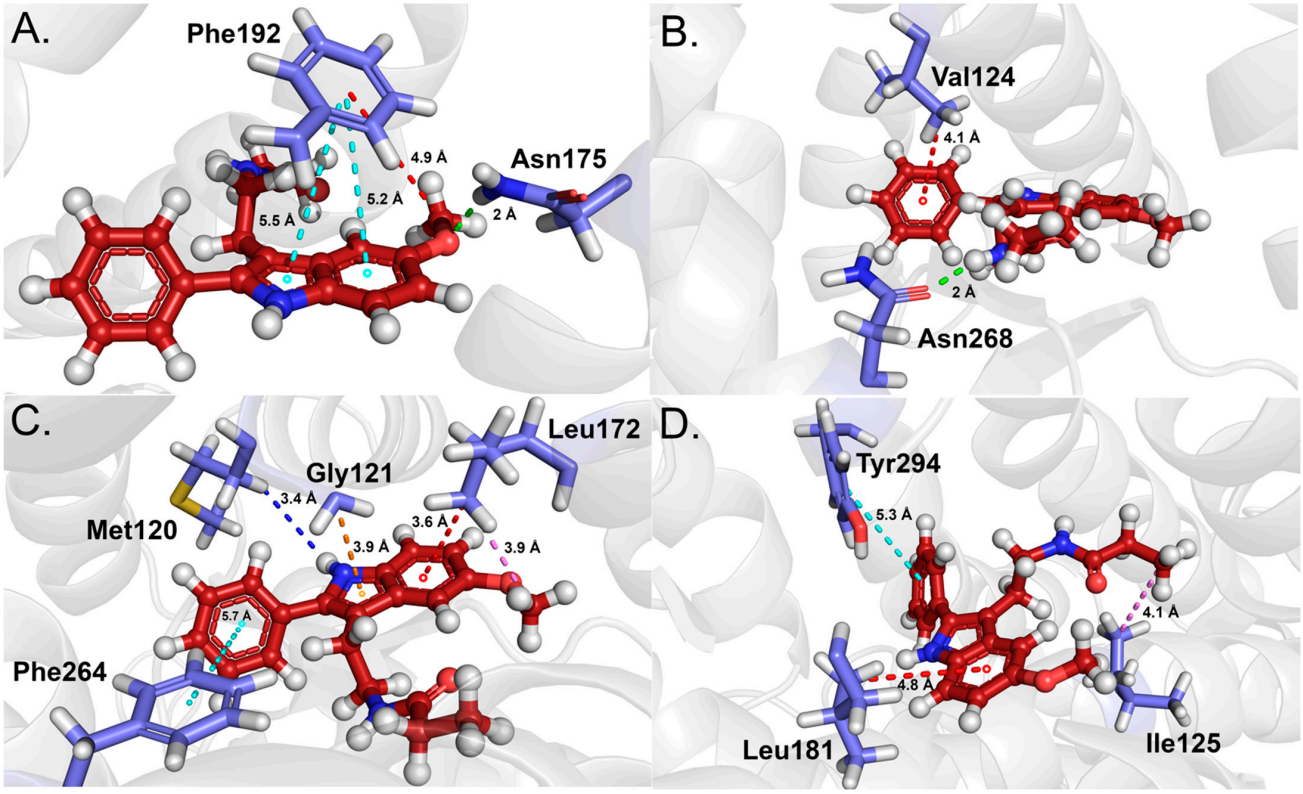

Figure 9 • An interaction analysis of the main amino acids of the MT_2-MPI complex. (**A**) An interaction analysis between MPI and the amino acid residues Asn 175 and Phe192. (**B**) An interaction analysis between MPI and amino acid residues Val124 and Asn268. (**C**) A representation of the interaction analysis between MPI and Met120, Gly121, Leu172, and Phe264. (**D**) An interaction analysis between the MPI ligand and the Ile125, Leu181, and Tyr294 amino acids. In all panels, the ligand is represented by a dark red ball-and-stick, and the main MT_1 amino acids are shown as pink sticks. The interaction type is colored as follows: pi–pi interaction (cyan); hydrogen bond (green); non-conventional hydrogen bond (dark blue); pi–alkyl interaction (red); alkyl–alkyl interaction (pink); and pi–hydrogen interaction (orange).

A pi–alkyl interaction is seen with the [C] ring in Val124 (−3.38 kcal/mol) (**Figure 9B**), similar to that seen with 2-PMT [28]. The amino acid exhibiting the third lowest interaction energy with MPI was Gly121 (−4.98 kcal/mol), which binds in a pi–hydrogen interaction with the [B] ring of the ligand (**Figure 9C**). Phe264 (−3.41 kcal/mol), the amino acid exhibiting the fifth most significant interaction with MPI, was involved in a pi–pi interaction in a "T" shape with the [C] ring (**Figure 9C**). This type of interaction occurs when the aromatic rings are oriented perpendicularly to one another, rather than being "stacked". The amino acid Leu172 (−3.02 kcal/mol) participates in two interactions: pi–alkyl (3.6 Å) and alkyl–alkyl (3.9 Å) (**Figure 9C**). An unusual hydrogen interaction with the ii(N)H atom has been identified at a distance of 3.4 Å for Met120 (−2.81 kcal/mol) (**Figure 9C**).

Tyr294 (−3.29 kcal/mol) is involved in pi–pi contact (5.3 Å) with the [C] ring, which is also noted in the interaction with 2-PMT (**Figure 9D**). Leu181 (−2.10 kcal/mol) interacts via pi–alkyl contact with the [A] ring at a distance of 4.8 Å, while Ile125 (−2.91 kcal/mol) exhibits an alkyl–alkyl interaction with the i(C1) atom at a distance of 4.1 Å (**Figure 9D**).

3.3. Quantum ligand properties

3.3.1. Energetic characterization

We fully measured several energy parameters for each of the four pharmaceutical compounds we studied (**Table 3**). The total energies of the compounds ranged from −810.42 to −1097.83 Ha, indicating the energies of the systems in their optimum electronic configurations. The total energy of MLT was −810.42 Ha, while the total energy of MPI was −1097.83 Ha (**Table 3**). The interaction energies ranged from −56.66 Ha (MLT) to −74.15 Ha (MPI).

We quantified the dipole moments of the compounds, indicating the distribution of charges within the molecules and their degree of polarization. The obtained values ranged from 2.66 Debye to 3.51 Debye, as seen in **Table 3**. MLT has a greater dipole moment, indicating that it is more polar. This influences its solubility in polar solvents and its interactions with biological targets. We measured the dielectric and solvation energies for each molecule, observing values of roughly −0.03 Ha for all compounds (**Table 3** and **Figure 9**). Consequently, the disparity in solubility for each drug can be mainly attributed to its molecular structure, as shown in a 2D drawing in Figure S8.

The surface areas, which provide information about the area of interaction of the compounds with the biological environment into which they are inserted, varied from 937.71 to 1162.24 $Å^2$. The cavity volumes, which represent the space located within the molecular structures, ranged from 1819.80 to 2511.48 $Å^3$. This information can be seen in **Table 3** and **Figure 10**.

Table 3 • Quantum energies of MLT, 2-PMT, RMT, and MPI.

Quantum energies							
Compound	**Total energy (Ha)**	**Binding energy (Ha)**	**Dipole mag**	**Dielectric energy (Ha)**	**Solvation energy (Ha)**	**Surface area**	**Cavity volume**
MLT	−810.42	−56.66	3.51	−0.03	−0.03	937.71	1819.8
2-PMT	−1056.11	−71.12	2.98	−0.03	−0.03	1140.49	2381.75
RMT	−877.38	−59.48	2.66	−0.03	−0.03	949.23	2033.99
MPI	−1097.83	−74.15	3.15	−0.03	−0.03	1162.24	2511.48

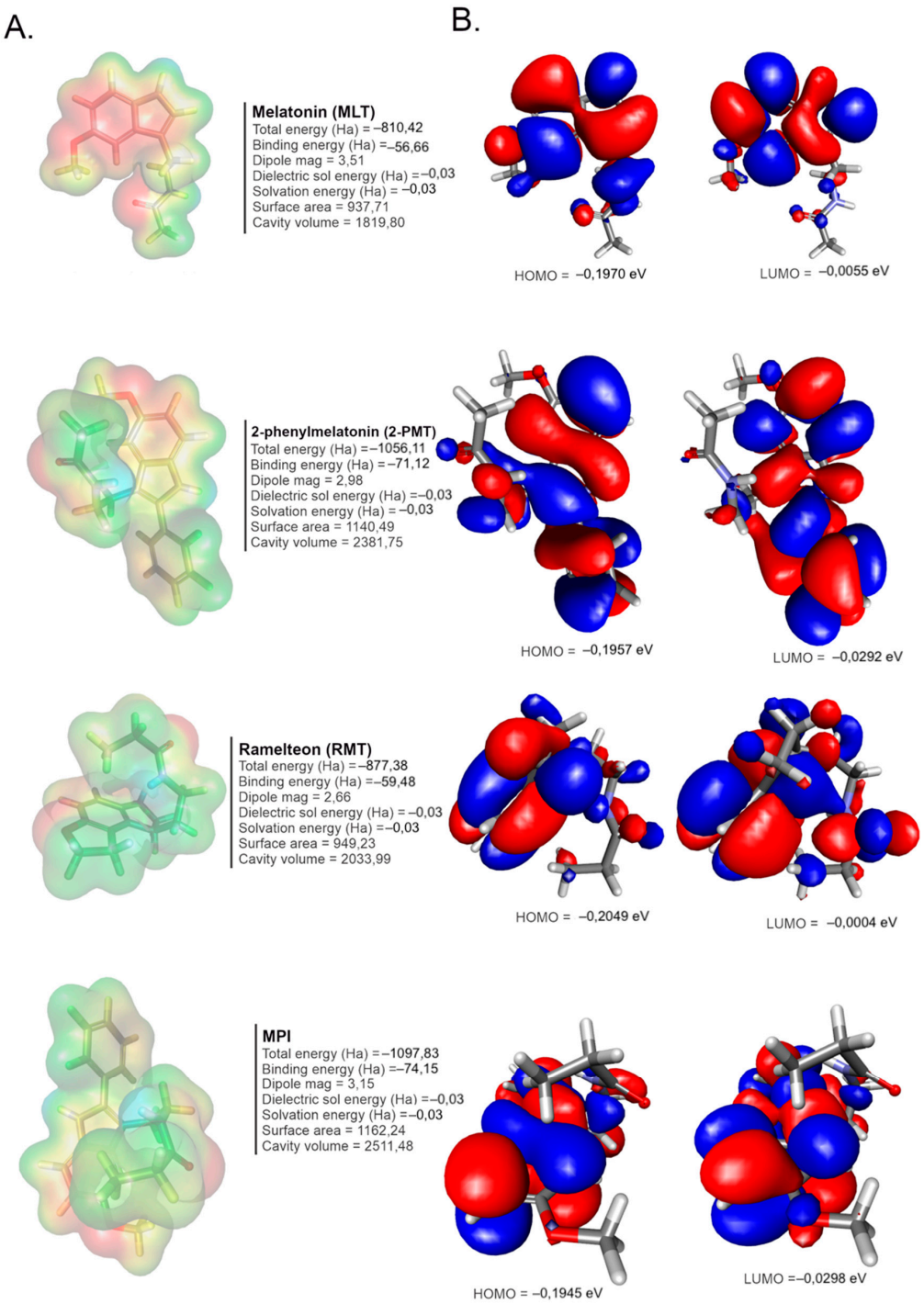

Figure 10 • (**A**) Molecular electrostatic potential (MEP) highlighting the charge distributions of each compound (**left**) and their quantum descriptors (**right**); (**B**) HOMO-LUMO orbitals and their respective energies.

3.3.2. Molecular electrostatic potential of optimized compounds

Molecular electrostatic potential (MEP) maps were generated to elucidate the electron density distribution in the examined compounds (**Figure 10A**), serving as a crucial instrument for visualizing areas of negative charge (negative electrostatic potentials) and positive charge (positive potentials).

In the investigated compounds, the areas of negative potential (shown in red in **Figure 10A**) are predominantly associated with oxygen and nitrogen atoms, suggesting regions susceptible to interactions with electrophilic substances. The areas of positive potential (shown in blue in **Figure 10A**) are mostly characterized by hydrogen atoms attached to heteroatoms, indicating areas suitable for interactions with nucleophilic molecules or regions.

The examination of quantum-chemical descriptors is crucial for comprehending the chemical reactivity and stability of the investigated pharmaceutical substances, as well as for aiding in the prediction of their biological function. The frontier molecular orbitals, designated as HOMO (Highest Occupied Molecular Orbital) and LUMO (Lowest Unoccupied Molecular Orbital), seen in **Figure 10B**, are crucial to the reactivity of substances and consequently their pharmacological effects.

MLT contains a HOMO-LUMO gap of 5.210 eV, indicating less chemical reactivity. The ionization potential (I) is 5.360 eV, and the electron affinity (A) is 0.150 eV. The chemical hardness (η) was 2.605 eV, whereas the softness (σ) was 0.384 eV. The chemical potential (μ) was 2.755 eV, while the electronegativity index (χ) was −2.755 eV. The electrophilicity index (ω) measures at 9.889 eV. These values are presented in **Table 4**.

Table 4 • Quantum-chemical descriptors of compounds: MLT, 2-PMT, RMT, and MPI.

Quantum-chemical descriptors (in eV)										
Compound	HOMO	LUMO	GAP	I [1]	A [2]	η [3]	σ [4]	μ [5]	χ [6]	ω [7]
MLT	−5.36	−0.15	−5.21	5.36	0.15	2.61	0.38	2.76	−2.76	9.89
2-PMT	−5.32	−0.80	−4.53	5.32	0.80	2.26	0.44	3.06	−3.06	10.60
RMT	−5.58	0.01	−5.59	5.58	−0.01	2.79	0.36	2.78	−2.78	10.81
MPI	−5.29	−0.81	−4.48	5.29	0.81	2.24	0.45	3.05	−3.05	10.43

[1] Ionization Potential (I), [2] Electronic Affinity (A), [3] Chemical Hardness (η), [4] Softness (σ), [5] Chemical Potential (μ), [6] Electronegativity (χ), [7] Electrophilicity Index (ω).

The molecule 2-PMT had a reduced HOMO-LUMO gap of 4.529 eV, signifying enhanced reactivity relative to that of MLT. The ionization potential is 5.325 eV, while the electron affinity is 0.796 eV. The chemical hardness is 2.264 eV, whereas the softness is 0.442 eV. The chemical potential is 3.060 eV, while the electronegativity index of 2-PMT is −3.060 eV. The electrophilicity index measures at 10.604 eV. These values are presented in **Table 4**.

RMT had the most substantial HOMO-LUMO gap of 5.587 eV, comparable to that of MLT; however, it was inferior to that for 2-PMT and was the compound with the least reactivity among those analyzed. An increased energy gap indicates that greater energy is necessary to elevate an electron from the HOMO to the LUMO, hence rendering the compound less likely to engage in chemical processes [72]. RMT possesses an ionization potential of 5.575 eV and an electron affinity of −0.012 eV, identifying it as the only molecule with a negative electron affinity, indicating a reduced tendency to accept electrons. Its chemical hardness is maximal at 2.793 eV, while its softness is minimal at 0.358 eV. The drug's chemical potential is 2.782 eV, and its electronegativity index is −2.782 eV. The electrophilicity index is 10.808 eV, as indicated in **Table 4**.

The MPI compound demonstrated the lowest HOMO-LUMO gap of 4.481 eV, indicating enhanced reactivity relative to that of the other compounds. A reduced gap signifies that the compound is more predisposed to involvement in chemical processes, as it requires less energy for the electronic transition. The ionization potential is 5.292 eV, while the maximum electron affinity is 0.811 eV, reflecting a pronounced propensity to receive electrons. The chemical hardness is minimal at 2.241 eV, whereas the softness is maximal at 0.446 eV. The chemical potential is 3.052 eV, while the electronegativity index is −3.052 eV. The electrophilicity index measures at 10.434 eV. All of these findings are presented in **Table 4**.

4. Discussion

Many studies rely on experimentally resolved structures without the need for conformational adjustments, as the analyzed data often align with the literature [26, 73–75]. However, in a recent study by our group on melatonin analogs (MLT), we encountered a protein–ligand complex for which the analyses did not corroborate with the existing literature. The results of density functional theory (DFT) calculations, a quantum-mechanical (QM) method, for the MT_1-RMT complex in that study did not align with the established findings, which assert that RMT has a higher affinity for the MT_1 receptor than that of MLT and a greater affinity for MT_1 than for MT_2 [76, 77]. Since this was the only complex among the six studied that did not match the experimental data, the issue appeared to lie with the MT_1-RMT complex.

The results presented indicate that the newly obtained complex exhibits an intermediate energy between those of MLT and 2-PMT, aligning with our expectations and consistent with previously reported findings in the literature [76, 77]. Another parameter that needed to be reviewed was the energy between RMT and the MT_1 and MT_2 proteins. According to in vitro experimental data, all of the molecules described in the literature have a higher affinity for MT_1 than for MT_2. As observed in the study by Menezes et al. (2024) [28], the MT_1-RMT^{XFEL} complex exhibited higher

binding energy than those of the MT_2-RMT complex, the opposite of the expected result. Once again, the model obtained from MD (MT_1-RMT^{MD}) yielded results more consistent with those in the literature, where RMT has a higher affinity for MT_1 than MT_2.

Many differences between the ligand mode of RMT^{MD} and RMT^{XFEL} were observed in our analysis. In previous analyses, Gly108, Val111, and Val191 were identified as necessary for the interaction with the MT_1 molecule [28]. In this complex, with the new conformation of the RMT molecule in the receptor, the affinity of these three amino acids increased, with Val191 showing a more subtle improvement. Overall, the adjustments made in the protein–ligand interactions resulted in a reduction of −14.76 kcal/mol in energy, leading to an increase in receptor–drug affinity. It is important to highlight that the significance of Phe179 was once again confirmed in this complex, as was the importance of Gly108, Val111, and Val191. However, Gln181 and Asn162 no longer appear among the ten most essential residues in the MT_1-RMT^{MD} complex.

These changes suggest that a conformational adjustment occurred, allowing for the formation of more favorable interactions while unfavorable ones were eliminated. Thus, the presented data may support the initial hypothesis that the experimental structure might not represent the lowest-energy conformation. In this case, the MD performed in the replicates was sufficient to optimize the conformation of the ligand and amino acid residues in the binding site for improved interaction between the molecules.

Moreover, these results are in accordance with previous studies that have shown that MD simulations can adjust the ligand binding modes to match experimental observations better, particularly in G protein-coupled receptors (GPCRs), where MD refinement improved the accuracy of ligand positioning compared to static crystal structures [78]. Indeed, MD simulations are widely recognized for enhancing the accuracy of protein–ligand binding mode assessments by evaluating the stability of various poses derived from crystallographic structures [79, 80]. Studies have shown that approximately 94% of native poses remain stable during simulations, demonstrating the reliability of MD in judging the stability of experimentally determined binding modes [81]. This highlights the value of MD simulations as a dependable tool for validating binding modes in structure-based drug design.

Unlike the other molecules and the QM/MM calculation, MPI showed greater affinity for MT_2 than for MT_1. Compared to 2-PMT, which was the best melatonin receptor agonist at the time, MPI had a small energy gain of −2.42 kcal/mol for the MT_1 receptor, with a dielectric constant of $\epsilon = 40$. Obtaining a lower energy value of −12.04 kcal/mol for the dielectric constant of $\epsilon = 40$ meant that the gain from the interaction with the MT_2 molecule was much bigger. Based on these results, MPI may be much better than the other molecules at changing the day/night phase, which is what the MT_2 receptor is supposed to do. And it may have a similar or a slightly greater efficacy than that of 2-PMT in reducing neuronal firing, the main function of the MT_1 receptor (**Table 2**). In any case, the MPI molecule appears to be a promising one in terms of its affinity for both melatonin receptors.

The recent interaction analysis revised the critical residues involved in the interaction among the four examined compounds. In MT_1, according to the current RMT analysis, the shared residues in the four ligand interaction analyses included Phe179, Gly108, Leu254, Met107, Val111, and Val191, with the single alteration being the exclusion of Ile112, which was identified within a 5 Å radius of the ligand in MPI. The amino acid that was configured as the only one in the interaction with MPI was His195.

In MT_2, the key amino acids involved in the interaction with the four ligands were Phe192, Val124, Gly121, Leu172, and Asn268, leading to the exclusion of Val204, which exhibited higher energy in its interaction with MPI. Despite this, Val204 interacts in two alkyl–alkyl interactions with two domains of MPI (i(C1) and ii(C12)). The amino acids exclusive to MPI include Phe264, Tyr294, and Leu181. Among these, only Leu181 fails to interact with the [C] ring or C1 derived from 2-PMT and RMT, respectively.

These data validate previous observations about the significance of the amino acid Phe179/Phe192 in the two MT receptors. Moreover, the amino acids Gly108/Gly121, Val111/Val124, and Val191/Val204 were demonstrated to be significant to the interaction with the four compounds. Excluding MLT from the study of common residues expands the list to Phe179/Phe192, Gly108/Gly121, Val111/Val124, Val191/Val204, and Met107/Met120. Val111, Met107, Ile112, and Ala104 have been suggested as important amino acids for providing a hydrophobic environment to improve the binding stability of gastrodin with MT_1 [82]. A recent study with another melatonin ligand, agomelatine, revealed the importance of the amino acids Gly108/Gly121 and Val111/Val124, as we observed here [83]. Hence, we suggest that these amino acids are important to the binding affinity and stability between ligands and melatonin proteins.

5. Conclusions

The present study demonstrated how MD simulations can effectively perform conformational adjustments, enabling more accurate analyses of protein–ligand interactions. MD simulations offer a powerful tool for enhancing the crystallographic structures of protein–ligand complexes. By providing insights into dynamic behavior, refining binding modes, and integrating with experimental data, MD contributes significantly to our understanding and utilization of these biomolecular interactions in research and drug development.

Based on this novel analysis and the previous data from MLT, 2-PMT, and RMT complex analyses, we have proposed a new molecular agonist for the MT_1 and MT_2 receptors: N-[2-(5-methoxy-2-phenyl-1H-indol-3-yl)ethyl]propanamide (MPI). This molecule was previously studied in *Xenopus laevis* melatonin receptors in 1995. However, human melatonin studies have not been described in the literature. In order to determine this molecule's potential effects on human receptors, we employed computational approaches that accurately ranked the compounds according to their affinity for melatonin receptors.

This study's findings revealed a molecule that bound more strongly to MT_1 and MT_2 than to MLT, RMT, or 2-PMT. In addition, MPI binds more strongly to MT_2 than MT_1, setting it apart from other melatonin receptor agonists and compounds. It can be inferred from this that MPI performs better during phase shifts (day/night). However, experimental analysis should be performed to confirm this finding.

Moreover, it was noted that MPI has a lower energy gap between the HOMO and the LUMO. A reduced energy difference

between the HOMO and the LUMO indicates enhanced reactivity, increasing the donation or acceptance of electrons in interactions with proteins or enzymes, hence enhancing the binding affinity and therapeutic efficacy of the compounds [66]. Consequently, it is proposed that MPI has significant therapeutic potential for stronger interactions with melatonin receptors.

This study demonstrated how molecular dynamics simulations can be utilized to refine crystallographic structures for the enhancement of protein–ligand interactions; however, it is essential to recognize their limitations. All research was conducted in an in silico environment, indicating that we simulated the biological system; therefore, the implementation of in vitro and in vivo experiments is essential to validate the observations made herein and to enhance this study's quality, including an assessment of the safety and specificity of MPI. Nonetheless, this study signifies progress in the formulation of a novel pharmacological intervention for insomnia management.

Acknowledgments

We would like to thank the Núcleo de Processamento de Alto Desempenho (NPAD) of the Federal University of Rio Grande do Norte for allowing us to use their computer facilities.

Funding

This research was partially sponsored by the Brazilian Research Agencies Coordenação de Aperfeiçoamento de Pessoal de Nível Superior (CAPES), Conselho Nacional de Desenvolvimento Científico e Tecnológico (CNPq) and the Center for Computational Engineering Sciences (CCES) at Unicamp under grant (FAPESP/CEPID Grant 2013/08293-7).

Author contributions

Conceptualization, G.d.L.M., J.I.N.O., U.L.F. and J.F.A.; methodology, G.d.L.M., G.V.R.d.S., K.S.B., D.S.G., R.A.d.S. and C.S.G.R.D.; formal analysis, G.d.L.M. and G.V.R.d.S.; validation, D.S.G., R.A.d.S. and U.L.F; investigation, G.d.L.M., M.V.S., G.V.R.d.S. and C.S.G.R.D.; writing—original draft preparation, G.d.L.M. and G.V.R.d.S.; writing—review and editing, K.S.B., M.V.S., R.A.d.S., J.F.A., J.I.N.O. and D.S.G.; visualization, K.S.B, G.d.L.M., G.V.R.d.S. and M.V.S.; supervision, U.L.F., J.F.A. and D.S.G.; funding acquisition, D.S.G. and U.L.F.; project administration, U.L.F. All authors have read and agreed to the published version of the manuscript.

Conflict of interest

The authors declare that they have no competing interests.

Data availability statement

The data supporting the findings of this publication has been made available within a publicly accessible repository at https://www.rcsb.org/structure/6ME2 (accessed on 2024 Jun 25): the XFEL structures of the MT1 and RMT molecules are available under Protein Data Bank data base accession code 6ME2; and at https://doi.org/10.5281/zenodo.14796596: the molecular structures obtained from MD and used for the DFT calculations and the input files for the MD and QM/MM calculations. Additional data supporting the findings of this publication can be made available upon request.

Supplementary materials

The Supplementary materials are available at https://doi.org/10.20935/AcadBiol7907. References [28, 84–88] are cited in the supplementary materials.

Additional information

Received: 2025-06-04

Accepted: 2025-09-11

Published: 2025-09-26

Academia Biology papers should be cited as *Academia Biology 2025*, ISSN 2837-4010, https://doi.org/10.20935/AcadBiol7907. The journal's official abbreviation is *Acad. Biol.*

Publisher's note

Copyright

References

1. Pandi-Perumal SR, Trakht I, Srinivasan V, Spence DW, Maestroni GJM, Zisapel N, et al. Physiological effects of melatonin: role of melatonin receptors and signal transduction pathways. Prog Neurobiol. 2008;85:335–53. doi: 10.1016/j.pneurobio.2008.04.001

2. Ma Z, Yang Y, Fan C, Han J, Wang D, Di S, et al. Melatonin as a potential anticarcinogen for non-small-cell lung cancer. Oncotarget. 2016;7:46768–84. doi: 10.18632/oncotarget.8776

3. Ishida N, Kaneko M, Allada R. Biological clocks. Proc Natl Acad Sci USA. 1999;96:8819–20. doi: 10.1073/pnas.96.16.8819

4. Reppert SM, Godson C, Mahle CD, Weaver DR, Slaugenhaupt SA, Gusella J. Molecular characterization of a second melatonin receptor expressed in human retina and brain:

the Mel1b melatonin receptor. Proc Natl Acad Sci USA. 1995;92:8734–8. doi: 10.1073/pnas.92.19.8734

5. Reppert SM, Weaver DR, Ebisawa T. Cloning and characterization of a mammalian melatonin receptor that mediates reproductive and circadian responses. Neuron. 1994;13:1177–85. doi: 10.1016/0896-6273(94)90055-8

6. Uz T, Arslan AD, Kurtuncu M, Imbesi M, Akhisaroglu M, Dwivedi Y, et al. The regional and cellular expression profile of the melatonin receptor MT1 in the central dopaminergic system. Mol Brain Res. 2005;136:45–53. doi: 10.1016/j.molbrainres.2005.01.002

7. Al-Ghoul WM, Herman MD, Dubocovich ML. Melatonin receptor subtype expression in human cerebellum. Neuroreport. 1998;9:4063–8. doi: 10.1097/00001756-199812210-00011

8. Clemens J, Jarzynka M, Witt-Enderby P. Down-regulation of mt1 melatonin receptors in rat ovary following estrogen exposure. Life Sci. 2001;69:27–35. doi: 10.1016/S0024-3205(01)01097-9

9. Frungieri MB, Mayerhofer A, Zitta K, Pignataro OP, Calandra RS, Gonzalez-Calvar SI. Direct effect of melatonin on Syrian hamster testes: melatonin subtype 1a receptors, inhibition of androgen production, and interaction with the local corticotropin-releasing hormone system. Endocrinology. 2005;146:1541–52. doi: 10.1210/en.2004-0990

10. Naji L, Carrillo-Vico A, Guerrero JM, Calvo JR. Expression of membrane and nuclear melatonin receptors in mouse peripheral organs. Life Sci. 2004;74:2227–36. doi: 10.1016/j.lfs.2003.08.046

11. Ozminkowski RJ, Wang S, Walsh JK. The direct and indirect costs of untreated insomnia in adults in the United States. Sleep. 2007;30:263–73. doi: 10.1093/sleep/30.3.263

12. Wardle-Pinkston S, Slavish DC, Taylor DJ. Insomnia and cognitive performance: a systematic review and meta-analysis. Sleep Med Rev. 2019;48:101205. doi: 10.1016/j.smrv.2019.07.008

13. Johnson KA, Gordon CJ, Chapman JL, Hoyos CM, Marshall NS, Miller CB, et al. The association of insomnia disorder characterised by objective short sleep duration with hypertension, diabetes and body mass index: a systematic review and meta-analysis. Sleep Med Rev. 2021;59:101456. doi: 10.1016/j.smrv.2021.101456

14. Thondala B, Pawar H, Chauhan G, Panjwani U. The effect of non-pharmacological interventions on sleep quality in people with sleep disturbances: a systematic review and a meta-analysis. Chronobiol Int. 2023;40:1333–53. doi: 10.1080/07420528.2023.2262567

15. De Mendonça FMR, De Mendonça GPRR, Souza LC, Galvão LP, Paiva HS, De Azevedo Marques Périco C, et al. Benzodiazepines and sleep architecture: a systematic review. CNS Neurol Disord—Drug Targets. 2023;22:172–9. doi: 10.2174/1871527320666210618103344

16. Cardinali DP, Srinivasan V, Brzezinski A, Brown GM. Melatonin and its analogs in insomnia and depression. J Pineal Res. 2012;52:365–75. doi: 10.1111/j.1600-079X.2011.00962.x

17. Auld F, Maschauer EL, Morrison I, Skene DJ, Riha RL. Evidence for the efficacy of melatonin in the treatment of primary adult sleep disorders. Sleep Med Rev. 2017;34:10–22. doi: 10.1016/j.smrv.2016.06.005

18. Nowell PD, Mazumdar S, Buysse DJ, Dew MA, Reynolds CF, Kupfer DJ. Benzodiazepines and zolpidem for chronic insomnia: a meta-analysis of treatment efficacy. Jama. 1997;278:2170–7. doi: 10.1001/jama.1997.03550240060035

19. Andersen LPH, Gögenur I, Rosenberg J, Reiter RJ. Pharmacokinetics of melatonin: the missing link in clinical efficacy? Clin Pharmacokinet. 2016;55:1027–30. doi: 10.1007/s40262-016-0386-3

20. Bologna C, Madonna P, Pone E. Efficacy of prolonged-release melatonin 2 mg (PRM 2 mg) prescribed for insomnia in hospitalized patients for COVID-19: a retrospective observational study. J Clin Med. 2021;10:5857. doi: 10.3390/jcm10245857

21. Wade AG, Ford I, Crawford G, McMahon AD, Nir T, Laudon M, et al. Efficacy of prolonged release melatonin in insomnia patients aged 55–80 years: quality of sleep and next-day alertness outcomes. Curr Med Res Opin. 2007;23:2597–605. doi: 10.1185/030079907X233098

22. Laudon M, Frydman-Marom A. Therapeutic effects of melatonin receptor agonists on sleep and comorbid disorders. Int J Mol Sci. 2014;15:15924–50. doi: 10.3390/ijms150915924

23. Krieger DM, Barros CASMD, Mello EF, Terra MB. Agonistas da melatonina no tratamento da insônia e da depressão. Debates Em Psiquiatr. 2014;4:12–7. doi: 10.25118/2236-918X-4-3-2

24. Knockenhauer KE, Copeland RA. The importance of binding kinetics and drug–target residence time in pharmacology. Br J Pharmacol. 2024;181:4103–16. doi: 10.1111/bph.16104

25. Proost JH, Wierda JMKH, Meijer DKF. An extended pharmacokinetic/pharmacodynamic model describing quantitatively the influence of plasma protein binding, tissue binding, and receptor binding on the potency and time course of action of drugs. J Pharmacokinet Biopharm. 1996;24:45–77. doi: 10.1007/BF02353510

26. Da Rocha JM, Campos DMDO, Esmaile SC, Menezes GDL, Bezerra KS, Da Silva RA, et al. Quantum biochemical analysis of the binding interactions between a potential inhibitory drug and the Ebola viral glycoprotein. J Biomol Struct Dyn. 2024;43:4753–69. doi: 10.1080/07391102.2024.2305314

27. Silva GVR, Ramos Reiniger KA, De Lima Menezes G, Bezerra KS, Galvão DS, Saivish MV, et al. Quantum mechanical analysis of newly synthesized HIV-1 protease inhibitors: evaluation of wild-type and resistant strain binding interactions. Phys Chem Chem Phys. 2024;26:26748–64. doi: 10.1039/D4CP02895C

28. Menezes G de L, Sales Bezerra K, Nobre Oliveira JI, Fontenele Araújo J, Soares Galvão D, Vogel Saivish M. Quantum mechanics insights into melatonin and analogs binding to melatonin MT1 and MT2 receptors. Sci Rep. 2024;14:10922. doi: 10.1038/s41598-024-59786-x

29. Heo L, Feig M. Experimental accuracy in protein structure refinement via molecular dynamics simulations. Proc Natl Acad Sci USA. 2018;115:13276–81. doi: 10.1073/pnas.1811364115

30. Fujinaga M, Gros P, Van Gunsteren WF. Testing the method of crystallographic refinement using molecular dynamics. J Appl Crystallogr. 1989;22:1–8. doi: 10.1107/S0021889888009550

31. Müller P. Practical suggestions for better crystal structures. Crystallogr Rev. 2009;15:57–83. doi: 10.1080/08893110802547240

32. Van Der Spoel D, Lindahl E, Hess B, Groenhof G, Mark AE, Berendsen HJC. GROMACS: fast, flexible, and free. J Comput Chem. 2005;26:1701–18. doi: 10.1002/jcc.20291

33. Pronk S, Páll S, Schulz R, Larsson P, Bjelkmar P, Apostolov R, et al. GROMACS 4.5: a high-throughput and highly parallel open source molecular simulation toolkit. Bioinformatics. 2013;29:845–54. doi: 10.1093/bioinformatics/btt055

34. Kagami M, Wilter A, Diaz A, Vranken WF. The ACPYPE web server for small-molecule MD topology generation. 2019 [accessed on 2024 Nov 12]. Available from: https://bio2byte.be/tool/.

35. Jorgensen WL, Chandrasekhar J, Madura JD, Impey RW, Klein ML. Comparison of simple potential functions for simulating liquid water. J Chem Phys. 1983;79:926–35. doi: 10.1063/1.445869

36. Valdés-Tresanco MS, Valdés-Tresanco ME, Valiente PA, Moreno E. gmx_MMPBSA: a new tool to perform end-state free energy calculations with GROMACS. J Chem Theory Comput. 2021;17:6281–91. doi: 10.1021/acs.jctc.1c00645

37. Miller BR, McGee TD, Swails JM, Homeyer N, Gohlke H, Roitberg AE. *MMPBSA.py*: an efficient program for end-state free energy calculations. J Chem Theory Comput. 2012;8:3314–21. doi: 10.1021/ct300418h

38. Pettersen EF, Goddard TD, Huang CC, Couch GS, Greenblatt DM, Meng EC, et al. UCSF chimera—a visualization system for exploratory research and analysis. J Comput Chem. 2004;25:1605–12. doi: 10.1002/jcc.20084

39. DeLano WL. PyMOL: an open-source molecular graphics tool. 2002 [accessed on 2024 Nov 12]. Available from: https://legacy.ccp4.ac.uk/newsletters/newsletter40/11_pymol.pdf.

40. Albuquerque E, Fulco UL, Caetano E, Freire V. Quantum chemistry simulation of biological molecules. Cambridge: Cambridge University Press; 2020. doi: 10.1017/9781108774956

41. Albuquerque ACC, Bezerra KS, De Fátima Vianna J, Batista SO, De Lima Neto JX, De Oliveira Campos DM, et al. In silico evaluation of the binding energies of androgen receptor agonists in wild-type and mutational models. J Phys Chem B. 2023;127:5005–17. doi: 10.1021/acs.jpcb.3c01103

42. Dantas DS, Oliveira JIN, Lima Neto JX, Da Costa RF, Bezerra EM, Freire VN, et al. Quantum molecular modelling of ibuprofen bound to human serum albumin. RSC Adv. 2015;5:49439–50. doi: 10.1039/C5RA04395F

43. Lima Neto JX, Vieira DS, De Andrade J, Fulco UL. Exploring the Spike-hACE 2 Residue–residue interaction in human coronaviruses SARS-CoV-2, SARS-CoV, and HCoV-NL63. J Chem Inf Model. 2022;62:2857–68. doi: 10.1021/acs.jcim.1c01544

44. Lima Neto JX, Bezerra KS, Barbosa ED, Oliveira JIN, Manzoni V, Soares-Rachetti VP, et al. Exploring the binding mechanism of $GABA_B$ receptor agonists and antagonists through in silico simulations. J Chem Inf Model. 2020;60:1005–18. doi: 10.1021/acs.jcim.9b01025

45. Lima Neto JX, Bezerra KS, Barbosa ED, Araujo RL, Galvão DS, Lyra ML, et al. Investigation of protein-protein interactions and hotspot region on the NSP7-NSP8 binding site in NSP12 of SARS-CoV-2. Front Mol Biosci. 2024;10:1325588. doi: 10.3389/fmolb.2023.1325588

46. Zhang DW, Zhang JZH. Molecular fractionation with conjugate caps for full quantum mechanical calculation of protein–molecule interaction energy. J Chem Phys. 2003;119:3599–605. doi: 10.1063/1.1591727

47. Frisch MJ, Trucks GW, Schlegel HB, Scuseria GE, Robb MA, Cheeseman JR, et al. Gaussian 16. Wallingford (CT): Gaussian, Inc.; 2016.

48. Adamo C, Cossi M, Rega N, Barone V. Chapter 12—new computational strategies for the quantum mechanical study of biological systems in condensed phases. In: Eriksson LA, editor. Theoretical and computational chemistry. Vol. 9. Amsterdam: Elsevier; 2001. p. 467–538. doi: 10.1016/S1380-7323(01)80013-3

49. Albuquerque EL, Fulco UL, Freire VN, Caetano EWS, Lyra ML, De Moura FABF. DNA-based nanobiostructured devices: the role of quasiperiodicity and correlation effects. Phys Rep. 2014;535:139–209. doi: 10.1016/j.physrep.2013.10.004

50. Car R. Introduction to density-functional theory and ab-initio molecular dynamics. Quant Struct-Act Relatsh. 2002;21:97–104. doi: 10.1002/1521-3838(200207)21:2\TU\textless{}97::AID-QSAR97\TU\textgreater{}3.0.CO;2-6

51. Grimme S. Semiempirical GGA-type density functional constructed with a long-range dispersion correction. J Comput Chem. 2006;27:1787–99. doi: 10.1002/jcc.20495

52. Bezerra KS, Fulco UL, Esmaile SC, Lima Neto JX, Machado LD, Freire VN, et al. Ribosomal RNA–aminoglycoside hygromycin b interaction energy calculation within a density functional theory framework. J Phys Chem B. 2019;123:6421–9. doi: 10.1021/acs.jpcb.9b04468

53. Vianna JF, Bezerra KS, Lima Costa AH, Barbosa ED, Lima Neto JX, Oliveira JIN, et al. New ethionamide boosters and EthR2: structural and energetic analysis. Phys Chem Chem Phys. 2021;23:23233–41. doi: 10.1039/D1CP02853G

54. Berman HM, Westbrook J, Feng Z, Gillilan G, Bhat TN, Weissig H, et al. The protein data bank. Nucleic Acids Res. 2000;28:235–42. doi: 10.1093/nar/28.1.235

55. Stauch B, Johansson LC, McCorvy JD, Patel N, Han GW, Huang X-P, et al. Structural basis of ligand recognition at the human MT1 melatonin receptor. Nature. 2019;569:284–8. doi: 10.1038/s41586-019-1141-3

56. Johansson LC, Stauch B, McCorvy JD, Han GW, Patel N, Huang X-P, et al. XFEL structures of the human MT2 melatonin receptor reveal the basis of subtype selectivity. Nature. 2019;569:289–92. doi: 10.1038/s41586-019-1144-0

57. Li H, Robertson A, Jensen J. Propka online. 2005 [accessed on 2024 Nov 12]. Available from: https://www.ddl.unimi.it/vegaol/propka.htm.

58. Huey R, Morris GM, Forli S. Using AutoDock 4 and AutoDock vina with AutoDockTools: a tutorial. La Jolla (CA): The Scripps Research Institute Molecular Graphics Laboratory; 2012.

59. GitHub Repos. Meeko: preparation of small molecules for AutoDock. 2022 [accessed on 2024 Nov 12]. Available from: https://pypi.org/project/meeko/0.3.1/.

60. Yang M, Bo Z, Xu T, Xu B, Wang D, Zheng H. Uni-GBSA: an open-source and web-based automatic workflow to perform MM/GB(PB)SA calculations for virtual screening. Brief Bioinform. 2023;24:bbad218. doi: 10.1093/bib/bbad218

61. Menezes GdL, Rolim G, Bezerra KS, Saivish MV, Ribeiro Dantas CSG, Galvão D, et al. Integrating classical and quantum mechanics in melatonin receptors for structure-guided drug design. 2025. doi: 10.5281/zenodo.14796596

62. Davies M, Nowotka M, Papadatos G, Dedman N, Gaulton A, Atkinson F, et al. ChEMBL web services: streamlining access to drug discovery data and utilities. 2015 [accessed on 2024 Nov 12]. Available from: https://www.ebi.ac.uk/chembl/.

63. Kim S, Chen J, Cheng T, Gindulyte A, He J, He S, et al. PubChem 2025 update. Nucleic Acids Res. 2025;53:D1516–25. doi: 10.1093/nar/gkae1059

64. Ahamed FMM, Chinnam S, Challa M, Kariyanna G, Kumer A, Jadoun S, et al. Molecular dynamics simulation, QSAR, DFT, molecular docking, ADMET, and synthesis of ethyl 3-((5-bromopyridin-2-yl)imino)butanoate analogues as potential inhibitors of SARS-CoV-2. Polycycl Aromat Compd. 2024;44:294–312. doi: 10.1080/10406638.2023.2173618

65. Towseef Ahmad H, Mohammed Ameen KK, Saleem H, Syed Ali Padusha M, Mashood Ahamed FM. Molecular structure determination, spectroscopic, quantum computational studies and molecular docking of 4-(E)-[2-(benzylamino)phenylimino) methyl-2]ethoxy phenol. J Biomol Struct Dyn. 2023;41:3574–90. doi: 10.1080/07391102.2022.2052354

66. Tayyeb JZ, Mondal S, Anisur Rahman M, Kumar S, Bayıl I, Akash S, et al. Identification of *Helicobacter pylori*-carcinogenic TNF-alpha-inducing protein inhibitors via daidzein derivatives through computational approaches. J Cell Mol Med. 2024;28:e18358. doi: 10.1111/jcmm.18358

67. Shahab M, De Farias Morais GC, Akash S, Fulco UL, Oliveira JIN, Zheng G, et al. A robust computational quest: discovering potential hits to improve the treatment of pyrazinamide-resistant *Mycobacterium tuberculosis*. J Cell Mol Med. 2024;28:e18279. doi: 10.1111/jcmm.18279

68. Thanikaivelan P, Subramanian V, Raghava Rao J, Unni Nair B. Application of quantum chemical descriptor in quantitative structure activity and structure property relationship. Chem Phys Lett. 2000;323:59–70. doi: 10.1016/S0009-2614(00)00488-7

69. Garratt PJ, Jones R, Tocher DA, Sugden D. Mapping the melatonin receptor. 3. design and synthesis of melatonin agonists and antagonists derived from 2-phenyltryptamines. J Med Chem. 1995;38:1132–9. doi: 10.1021/jm00007a010

70. Rodham DA, Suzuki S, Suenram RD, Lovas FJ, Dasgupta S, Goddard WA, et al. Hydrogen bonding in the benzene–ammonia dimer. Nature. 1993;362:735–7. doi: 10.1038/362735a0

71. Zhang X, Dai H, Yan H, Zou W, Cremer D. B–H···π interaction: a new type of nonclassical hydrogen bonding. J Am Chem Soc. 2016;138:4334–7. doi: 10.1021/jacs.6b01249

72. Adindu EA, Godfrey OC, Agwupuye EI, Ekpong BO, Agurokpon DC, Ogbodo SE, et al. Structural analysis, reactivity descriptors (HOMO-LUMO, ELF, NBO), effect of polar (DMSO, EtOH, H_2O) solvation, and libido-enhancing potential of resveratrol by molecular docking. Chem Phys Impact. 2023;7:100296. doi: 10.1016/j.chphi.2023.100296

73. Lima Costa AH, Bezerra KS, De Lima Neto JX, Oliveira JIN, Galvão DS, Fulco UL. Deciphering interactions between potential inhibitors and the *Plasmodium falciparum* DHODH enzyme: a computational perspective. J Phys Chem B. 2023;127:9461–75. doi: 10.1021/acs.jpcb.3c05738

74. Campos DMO, Bezerra KS, Esmaile SC, Fulco UL, Albuquerque EL, Oliveira JIN. Intermolecular interactions of cn-716 and acyl-KR-aldehyde dipeptide inhibitors against Zika virus. Phys Chem Chem Phys. 2020;22:15683–95. doi: 10.1039/D0CP02254C

75. Bezerra EM, de Alvarenga ÉC, dos Santos RP, de Sousa JS, Fulco UL, Freire VN, et al. Losartan as an ACE inhibitor: a description of the mechanism of action through quantum biochemistry. RSC Adv. 2022;12:28395–404. doi: 10.1039/D2RA04340H

76. Miyamoto M. Pharmacology of ramelteon, a selective MT1/MT2 receptor agonist: a novel therapeutic drug for sleep disorders. CNS Neurosci Ther. 2009;15:32–51. doi: 10.1111/j.1755-5949.2008.00066.x

77. Nosjean O, Nicolas J-P, Klupsch F, Delagrange P, Canet E, Boutin JA. Comparative pharmacological studies of melatonin receptors: MT1, MT2 and MT3/QR2. Biochem Pharmacol. 2001;61:1369–79. doi: 10.1016/S0006-2952(01)00615-3

78. Kapla J, Rodríguez-Espigares I, Ballante F, Selent J, Carlsson J. Can molecular dynamics simulations improve the structural accuracy and virtual screening performance of GPCR models? PLoS Comput Biol. 2021;17:e1008936. doi: 10.1371/journal.pcbi.1008936

79. Zanatta G, Della Flora Nunes G, Bezerra EM, Da Costa RF, Martins A, Caetano EWS, et al. Two binding geometries for risperidone in dopamine D3 receptors: insights on the fast-off mechanism through docking, quantum biochemistry, and molecular dynamics simulations. ACS Chem Neurosci. 2016;7:1331–47. doi: 10.1021/acschemneuro.6b00074

80. Zanatta G, Nunes G, Bezerra EM, Da Costa RF, Martins A, Caetano EWS, et al. Antipsychotic haloperidol binding to the human dopamine D3 receptor: beyond docking through QM/MM refinement toward the design of improved schizophrenia medicines. ACS Chem Neurosci. 2014;5:1041–54. doi: 10.1021/cn500111e

81. Liu K, Kokubo H. Exploring the stability of ligand binding modes to proteins by molecular dynamics simulations: a cross-docking study. J Chem Inf Model. 2017;57:2514–22. doi: 10.1021/acs.jcim.7b00412

82. Zhang L, Lan M, Chen H, Ward R, Zhao Y, Guo J, et al. Activation of the melatonin receptor MT_1 by the natural product gastrodin to promote sleep. J Pineal Res. 2024;76:e70016. doi: 10.1111/jpi.70016

83. Cantarini M, Rusciano D, Amato R, Canovai A, Cammalleri M, Monte MD, et al. Structural basis for agonistic activity and selectivity toward melatonin receptors hMT1 and hMT2. Int J Mol Sci. 2023;24:2863. doi: 10.3390/ijms24032863

84. Berendsen HJC, Postma JPM, van Gunsteren WF, DiNola A, Haak JR. Molecular dynamics with coupling to an external bath. J Chem Phys. 1984;81:3684–90. doi: 10.1063/1.448118

85. Hutter J. Car-parrinello molecular dynamics: car-parrinello molecular dynamics. Wiley Interdiscip Rev Comput Mol Sci. 2012;2:604–12. doi: 10.1002/wcms.90

86. Hess B, Bekker H, Berendsen HJC, Fraaije JGEM. LINCS: a linear constraint solver for molecular simulations. J Comput Chem. 1997;18:1463–72. doi: 10.1002/(SICI)1096-987X(199709)18:12\TU\textless{}1463::AID-JCC4\TU\textgreater{}3.0.CO;2-H

87. Hess B. P-LINCS: a parallel linear constraint solver for molecular simulation. J Chem Theory Comput. 2008;4:116–22. doi: 10.1021/ct700200b

88. Hockney RW, Goel SP, Eastwood JW. Quiet high-resolution computer models of a plasma. J Comput Phys. 1974;14:148–58. doi: 10.1016/0021-9991(74)90010-2